Using small robotic telescopes to monitor Cepheid variable stars

Adam Bugg

A senior thesis submitted to the faculty of
Brigham Young University
in partial fulfillment of the requirements for the degree of

Bachelor of Science

Eric G. Hintz, Advisors

Department of Physics and Astronomy

Brigham Young University

ABSTRACT

Using small robotic telescopes to monitor Cepheid variable stars

Adam Bugg
Department of Physics and Astronomy, BYU
Bachelor of Science

Spectroscopic observations from the Dominion Astrophysical Observatory of the Cepheid X Cyg show that the star underwent a temperature shift and phase transition sometime between 2013 and 2014. As follow-up work, we conducted a photometric campaign to monitor X Cyg and a collection of 40 other Cepheids, measuring their temperature via a set of Hα filters in addition to the Johnson V filter. While phasing observations in the V filter reproduced clear light curves, Hα light curves were far less successful. The greatest hindrance to properly measuring Hα indices was likely poor signal-to-noise in the narrow Hα filter; the 8-inch telescope used may simply be unable to collect enough light. Accumulating more data, however, would likely reduce scatter and tighten up the results.

Keywords: Variable stars, Cepheids, Instrumentation, Photometry

ACKNOWLEDGMENTS

I thank my advisor, Dr. Eric Hintz, first for helping me convert greed for free money into a productive, two-year scientific endeavor; second for tolerating my at times incessant door knocking and question asking; and third for putting up with my admittedly and unexcusably poor understanding of how to decently tie a proper knot. I also thank the Office of Research and Creative Activities and the BYU Physics Department for providing funding for this research. In addition, I thank all the Astronomy faculty at BYU for fostering a welcoming and supportive educational environment. Finally, I thank my friends and family, especially my parents, for their constant encouragement and support.

Contents

Chapter 1

Introduction

1.1 History of variable stars

Most stars undergo variations in brightness or color over their lifetimes, but some have variations that can be observed on human timescales—remarkably fast compared to the lifetime of a star. These variations come in many different forms. Some are periodic, others irregular; some occur over the course of a few minutes, others take more than a century. The physical mechanisms governing variability also differ. Some stars pulsate, others are eruptive or even cataclysmic. Still others are variable due to their rotation or because an eclipsing companion blocks their light from view. To further complicate things, a system can be variable for more than one reason, and thus may belong to more than one class of variable star. Further, classification systems are far from standard across the field of astronomy. The General Catalogue of Variable Stars (GCVS), for example, lists over a hundred distinct types of variability. So many factors come into play to determine the way a star's brightness changes, in fact, that the classification of variable stars can be considered a rich, independent science unto itself.

The history of variable star discoveries and research is equally rich and complex. The first

confirmed discovery of a variable star in modernity was o Ceti by Johannes Holwarda in 1638. Later, in 1669, Algol was discovered to be variable by Geminiano Montanari, although recent analysis of the Calendar of Lucky and Unlucky Days (c. 1225 BC) shows that ancient Egyptians may have been aware of Algol's variable nature (Sterken & Jaschek 1996). Throughout the rest of the 17th and 18th centuries, several new variable stars would be detected by eye, but it was not until the advent of photographic measurement that low-amplitude variability could be accurately recorded. Since then, many variable stars have been discovered and catalogued—the current edition of the GCVS contains information on more than 50,000 variable objects!

With so many variable stars being discovered, a system of classification soon became necessary. The first attempt at classification of variable stars was done by Pickering at around the turn of the 20th century. The proposed classification system consisted of five classes: new stars, long-periodic variables, irregular variables, short-period variables, and eclipsing variables (Sterken & Jaschek 1996). Because so little was understood about the physical processes that cause variation, the classification system was based solely on observation. Eventually a more standardized system of variable classification developed, focusing first on whether a star's variability is intrinsic—due to processes internal to the star—or extrinsic—where a star's brightness doesn't actually change, but rather the variation in received flux is caused by some external factor, such as an eclipsing object.

The largest branch of variable stars is that of Cepheids. Cepheids are regularly pulsating stars that typically pulsate over the course of a few days or weeks. Historically, the term Cepheid was applied to any continuously varying star with a regular light curve and period less than about a month, unless it was known to be an eclipsing star (Feast 1996). Now, however, Cepheids are generally considered to be pulsating stars with periods of 1-50 days (though, some have periods as long as several months). The shape of Cepheids' light curves can also vary based on their periods. The light curves of long-period Cepheids often have steep rising branches, but the light curves of the longest period Cepheids of more than 40 days appear almost perfectly sinusoidal (Feast 1996).

Classifying Cepheids to their exact subclass cannot usually be done with the light curve alone; rather other information such as galactic position, radial velocity, and chemical composition is needed.

In this project, we monitored a collection of Cepheids using robotic telescopes put in place on the observation deck of the Eyring Science Center. In particular, we attempted to track their temperature by measuring the strength of the Hα spectral line through a photometric system described in Section 1.6. Further discussion on the background and incentives for this project follow in the subsequent sections of the introduction. In Chapter 2, I detail the methods we employed to go about the study. Then I discuss the results and give recommendations for future work in Chapter 3.

1.2 Pulsation mechanism

Though no doubt the question of what drives the oscillations seen in pulsating variables such as Cepheids had arisen since their first discovery, surprisingly little research had been done on the matter until the mid-20$^{\text{th}}$ century. The first type of pulsation to be seriously investigated was radial pulsation in the 1940s (Cox 1985). One of the conclusions drawn from that investigation was that the amplitudes of pulsations deep in the interior of a star are quite small—so small, in fact, that nuclear reactions from the star's core could not be causing pulsation (Engle & Guinan 2012). Rather, pulsation must be the result of something happening in the envelope.

As it is currently understood, the primary driving mechanism behind the pulsation of Cepheids and other kinds of variable stars is the κ-mechanism, first introduced by Eddington (1941) and given its current name by Baker & Kippenhahn (1962), where κ represents radiative opacity. In a typical star, any increase in temperature and density causes a corresponding decrease in opacity, allowing energy to flow out more quickly and for the star to maintain thermodynamic equilibrium. But if for some reason opacity instead increases as a star is compressed, then heat flow is restricted, and the resulting pressure buildup inside a star's atmosphere pushes the outer layers back, resulting

in regular, periodic pulsation (Baker & Kippenhahn 1962). In Cepheids, that pressure buildup is caused by ionized material that brings heat into the outer layers during compression and releases heat during expansion. The ionizing material creates a destabilizing effect in a layer of the envelope by causing the local temperature to be lower than it would be without ionization (Cox 1985). Ionized gas has more degrees of freedom, so the energy added during compression goes into the degrees of freedom instead of thermal kinetic energy (Cox 1985). Opacity normally is inversely proportional to the cube of temperature, but because the temperature remains more or less constant, opacity increases instead of decreasing during compression, trapping energy that tries to get out.

For regular pulsation to occur, several criteria must be satisfied. First, a star needs enough ionizing material (in Cepheids, about 10-15% abundance), and second, that material must be in a layer of the star where behavior is transitioning from adiabatic to non-adiabatic (Engle & Guinan 2012). In Cepheids, the ionizing material is He II, which ionizes to He III at temperatures of 35,000-55,000 K (Engle & Guinan 2012). The depth in the star's atmosphere at which this temperature is reached depends on the spectral type of the star—in hot stars, that layer is close to the surface, while in cool stars, it is found closer to the core. The combination of these criteria are restrictive enough that Cepheids can only be found on a specific part of the Hertzsprung-Russel diagram, known as the instability strip (cf. Fig. 1.1).

The regularity of Cepheid pulsation has proved an invaluable tool over the years. In 1912, while working at the Harvard Observatory, Henrietta Leavitt noticed that the magnitudes of Cepheids in the Small Magellanic Cloud were related to their periods (Leavitt & Pickering 1912), (cf. Fig. 1.2). This so-called "Leavitt Law" has been quantified and calibrated over the years and is dependent also on a Cepheid's temperature, metallicity, and other factors. In general, however, it follows the form given by Saio & Gautschy (1998):

$$\log_{10}(L/L_{\odot}) \approx 2.5 + 1.25 \log_{10} P, \tag{1.1}$$

where P is the period in days, L is the luminosity of the star, and $L_{\odot}$ is solar luminosity.

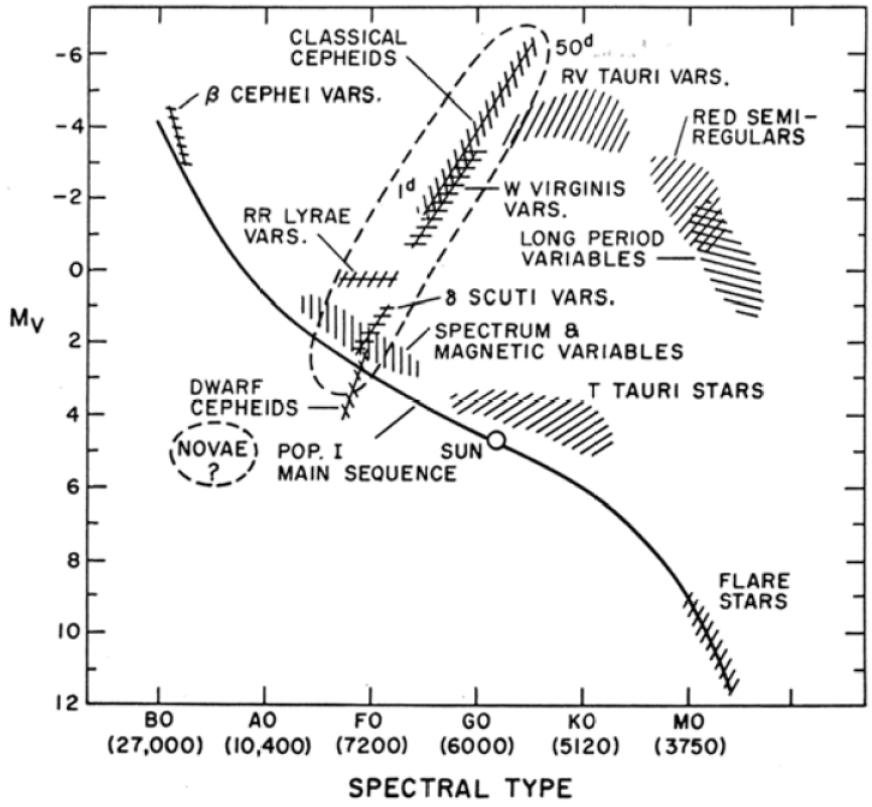

Figure 1.1 Hertzsprung-Russel Diagram, from Engle & Guinan (2012). The instability strip is outlined with dashes.

Using this relation, once a Cepheid's period of pulsation is measured, its intrinsic brightness can be determined. Then, once the absolute magnitude is known, the distance to the star can easily be calculated using the *distance modulus equation*:

$$m - M = 5\log_{10}(d) - 5, \tag{1.2}$$

where m is apparent magnitude, M is absolute magnitude, and d is distance, measured in parsecs. Thus Cepheids have become invaluable as standard candles in determining distances not only to other stars in our own galaxy, but to other galaxies as well.

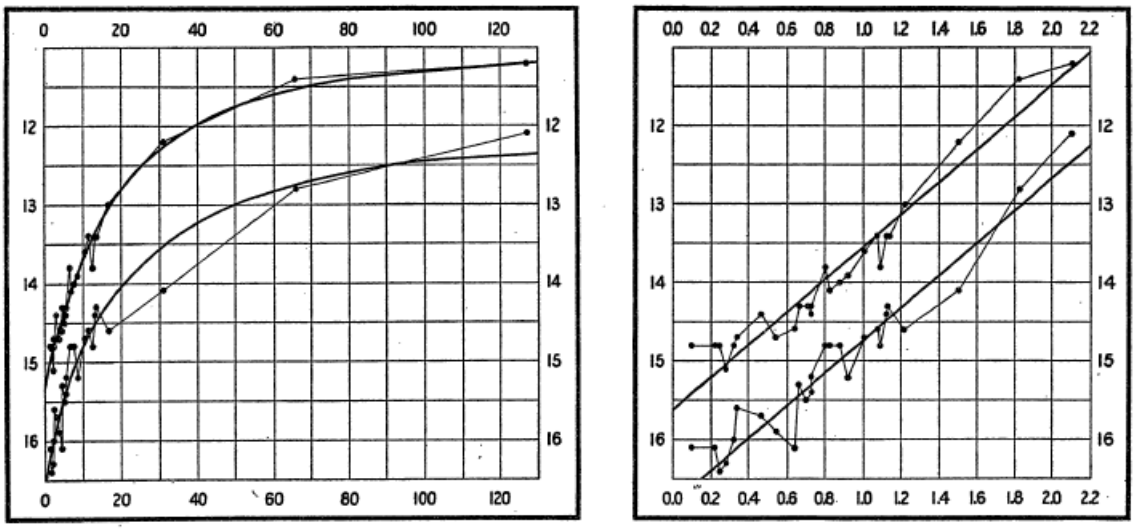

Figure 1.2 Period-Luminosity relation as reported in Leavitt & Pickering (1912). In the left panel, P (horizontal axis) is plotted against magnitude (vertical axis). In the right panel, $\log_{10} P$ is plotted instead. The two curves represent data taken at maximum and at minimum light.

1.3 Incentive for using robots

As explained in section 1.1, Cepheids are pulsating variable stars with periods of days or weeks. As such, it is impossible to obtain a complete light curve for a star over the course of a single night. The Cepheid X Cyg, for instance, takes about 16 days to complete its pulsation period (Samus et al. 2017). Naturally, constantly observing X Cyg for the entire 16-day period is impossible, as observations can only be made during the night—and only on nights with good weather, at that! In addition, taking observations every few minutes would be an inappropriate cadence for generating a light curve; X Cyg's light output doesn't change much on such a small time scale.

The solution to this problem, then, is to take only a few observations on a given night—often only one. Then, we can phase up our observations using known periods to see at what point in the cycle any given observation was taken. The advantage to such a position, then, is that we can observe many different Cepheids over the course of a single night. However, manually moving a

telescope to each target, centering it, taking a single observation, and then moving on to the next target would be inefficient, tedious, and cumbersome.

To alleviate the manpower required to observe so many targets and shorten the amount of time to move between them, we installed robotic telescopes that would be able automatically to center themselves on a target, take data, and then move to the next target. Fortunately, BYU already had several small telescopes on hand that were not currently being used. Using these smaller telescopes allowed us to observe bright Cepheids that other observatories cannot conduct research on without overexposing their camera equipment (see page 24).

Robotic telescopes also have other advantages over manually operated telescopes. A critical part of observational astronomy in the optical regime is data calibration, explained in Sections 2.4 and 2.5. One kind of calibration frame, known as a flat, requires a dim but uniform source of light across the entire CCD chip. Typically, these frames are taken during twilight, when the light level of the sky is bright enough to illuminate the entire CCD, but dim enough not to oversaturate the chip. But as the sun goes down at sunset, the sky, of course, grows dimmer. This means that the exposure length of these flat frames must constantly be lengthened to ensure an equal amount of light across each picture. Doing this manually is difficult and prone to errors. However, a robotic system can automatically scan each frame to see how much light was collected, then lengthen or shorten the exposure length of the next frame to correspond to the change in light level. This results in much higher quality flat frames.

1.4 Spectroscopy vs photometry

Spectroscopy and photometry are two fundamentally different types of observation. While spectroscopy involves taking a full spectrum of an object's emission, photometry uses filters to let light of a band of wavelengths in to the camera. A spectrograph uses a grating or prism to spread the

object's light across a row of pixels, separating different wavelengths of light. Photometry, on the other hand, groups photons of many wavelengths together. The Johnson V filter, for instance, allows light of wavelengths between about 500 nm and 650 nm, with peak efficiency at about 548 nm.

Spectroscopy and photometry each have their uses and drawbacks. Spectroscopy provides the most detailed information about a star's composition and lets us most accurately measure the strength of spectral lines. Photometry gives less detailed information, since photons of different wavelengths are grouped together. Although simultaneous photometric observations in enough filters essentially produces extremely low-resolution spectroscopy, only general information such as color differences between filters can usually be determined. However, spectrographs are expensive, with low-end products costing several thousand dollars. Photometric filters, on the other hand, are decidedly cheaper, typically costing only a few hundred dollars. Photometry also requires a lower signal-to-noise ratio (S/N) than spectroscopy, as the signal from the object is not being split apart and spread out across the CCD. So, the same size telescope can observe fainter stars photometrically than it can spectroscopically. Thus, while obtaining a spectrum provides more detailed information about a given target, sometimes photometric observations are sufficient.

The spectral feature of interest in this study was the Hα absorption line in Cepheids. While obtaining full spectra of the stars would have provided the best measurements, the monetary and S/N costs made a spectroscopic campaign prohibitive. Instead, we took far more cost effective observations photometrically, using a set of filters to isolate the Hα line. This system of filters is presented in Section 1.6.

1.5 Hα and temperature

An explanation of the connection between Hα and temperature requires a brief digression into the history of spectral classification. When Edward C. Pickering was appointed director of Harvard

College Observatory in 1877, he started a visual photometry program, personally making roughly 1,400,000 observations (Hearnshaw 1986b). Later, the recently-widowed Anna Palmer Draper approached Pickering with the desire to establish a spectroscopy program at Harvard as a memorial for her late husband Henry (Hearnshaw 1986b). The task of looking through the 28,266 classifiable spectra and organizing them fell on Mrs. Williamina P. Fleming, who had been working at the observatory as a computer and copyist (Hearnshaw 1986b). In 1890, Pickering published the results of this work as the Draper Memorial Catalogue of 10351 stars (Pickering 1890), classifying the spectra into types A-Q (except the letter J). The spectral types were based on several criteria—the strength of hydrogen absorption lines, the presence of helium lines, or simply the number of lines visible (Hearnshaw 1986b).

Later, Antonia Maury (Henry Draper's niece) came under the employment of Pickering and created a new classification scheme, using higher-resolution spectra than those used for the Draper Memorial Catalogue (Hearnshaw 1986b). This new system grouped the spectra by Roman numerals I-XXII based on the strength of their hydrogen lines, with the strongest lines corresponding to the first groups (Hearnshaw 1986b). Annie Jump Cannon then also began working at Harvard College Observatory and made her own classification system, combining the work of both Fleming and Maury (Hearnshaw 1986b). Without even referring to temperature, she grouped the spectra into the sequence: O, B, A, F, G, K, M, justifying her grouping primarily by the strength of the hydrogen lines (Hearnshaw 1986b). This system of spectral classification has persisted since then.

Although the connection between spectral types and temperature had long been suspected, it was not until 1905 that it was confirmed. The German astronomers J. Wilsing and J. Scheiner studied 109 stars across all spectral types, finding the hottest star a B type star and the coolest stars M types (Hearnshaw 1986a). Simultaneously, Charles Nordmann was working on the problem at the Paris Observatory. He determined temperatures for 14 stars, also showing the trend that O and B stars are hotter than K and M stars (Hearnshaw 1986a). Finally, in 1921, Megh Nad Saha derived

a quantitative temperature scale for every spectral type, showing clearly that temperature varies in an unbroken chain across the types—hot for O and B stars, cool for K and M stars.

So, the clear relationship between temperature and spectral type, which is determined by the strength of Hydrogen lines, means that the strength of a star's Hydrogen lines such as Hβ or Hα acts as a good indicator of its temperature. The Hydrogen lines are strongest in A type stars, then begin to fall off on either side. Since Cepheids are all located on the instability strip, their spectral types never cross over into the hot O or B stars. Thus, when we measure a strong Hα line, it clearly indicates a high temperature.

1.6 Goal of the project and previous work

The strength of the Hα absorption line can be measured from spectral data by examining the spectrum and determining the line's equivalent width (EW). The EW is found by creating a rectangle with the same height and area as the absorption feature in the spectrum. The width of that rectangle is the EW. Mathematically, the it can by found by

$$EW = \int (1 - F_\lambda / F_0) d\lambda, \tag{1.3}$$

where F_λ is the intensity at a given wavelength, and F_0 is the intensity of the continuum, before the absorption line.

However, the absorption line can also be measured spectrophotometrically by convolving[1] photometric filter response curves onto spectral data to determine the object's brightness in a given filter. To measure the Hα line, Joner & Hintz (2015) developed a photometric system of two filters—one wide and one narrow, whose response curves are shown in Figure 1.3. They then used this filter system to establish an Hα index, whereby the strength of the Hα line can be measured photometrically by subtracting the magnitude in the wide filter from that in the narrow.

[1] For details, see the documentation for the *sbands* command in IRAF.

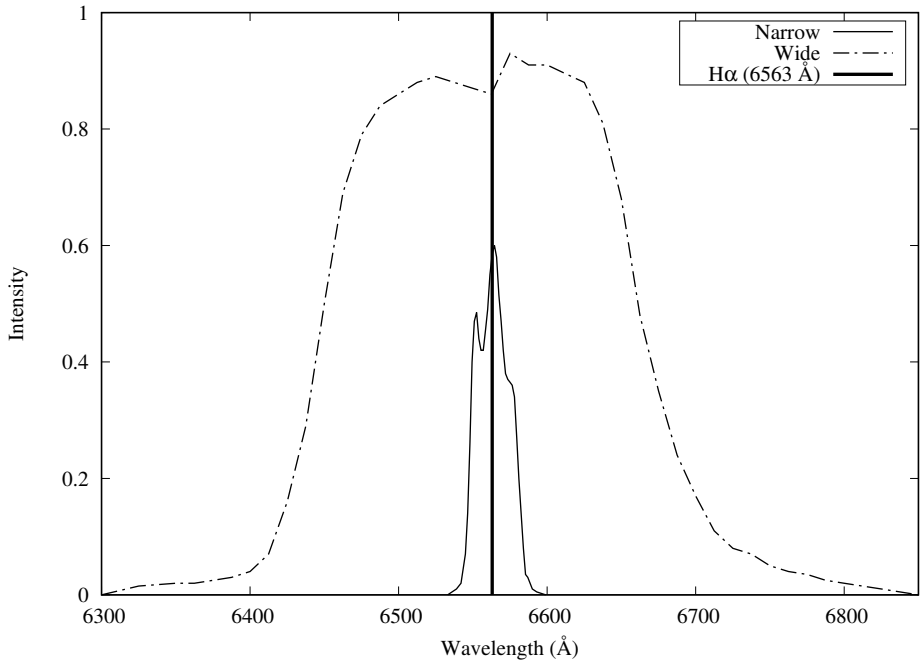

Figure 1.3 Intensity of the wide and narrow filters centered around the H-α spectral line. Data for the curves taken from Joner & Hintz (2015).

Once the Hα index is measured, the temperature can be found. The exact relation between calibrated Hα index (H_α) and surface temperature (T_{eff}) in Kelvin was presented by Joner & Hintz (2015). For stars cooler than type A2, which includes all of the stars in this study, the relation is $T_{\rm eff} = 5040/\theta$, where

$$\begin{aligned}\theta = &- 162.627(41.215) * H_\alpha^4 + 1751.335(455.374) * H_\alpha^3 \\ &- 7063.688(1886.200) * H_\alpha^2 + 12644.249(3471.369) * H_\alpha - 8473.302(2395.089).\end{aligned} \tag{1.4}$$

Using this filter system, spectrophotometric observations from the 1.2-meter McKellar telescope at the Dominion Astrophysical Observatory (DAO) show that between 2013 and 2014, the Cepheid X Cyg underwent an unexpected drop in temperature. Figure 1.4 shows the difference in Hα index values before and after the temperature drop. As follow-up work, we began a purely photometric campaign, using the Hα filters to monitor the temperature of X Cyg and 40 other Cepheids.

The goal of this project was two-fold: First, we aimed to monitor the temperature of Cepheids

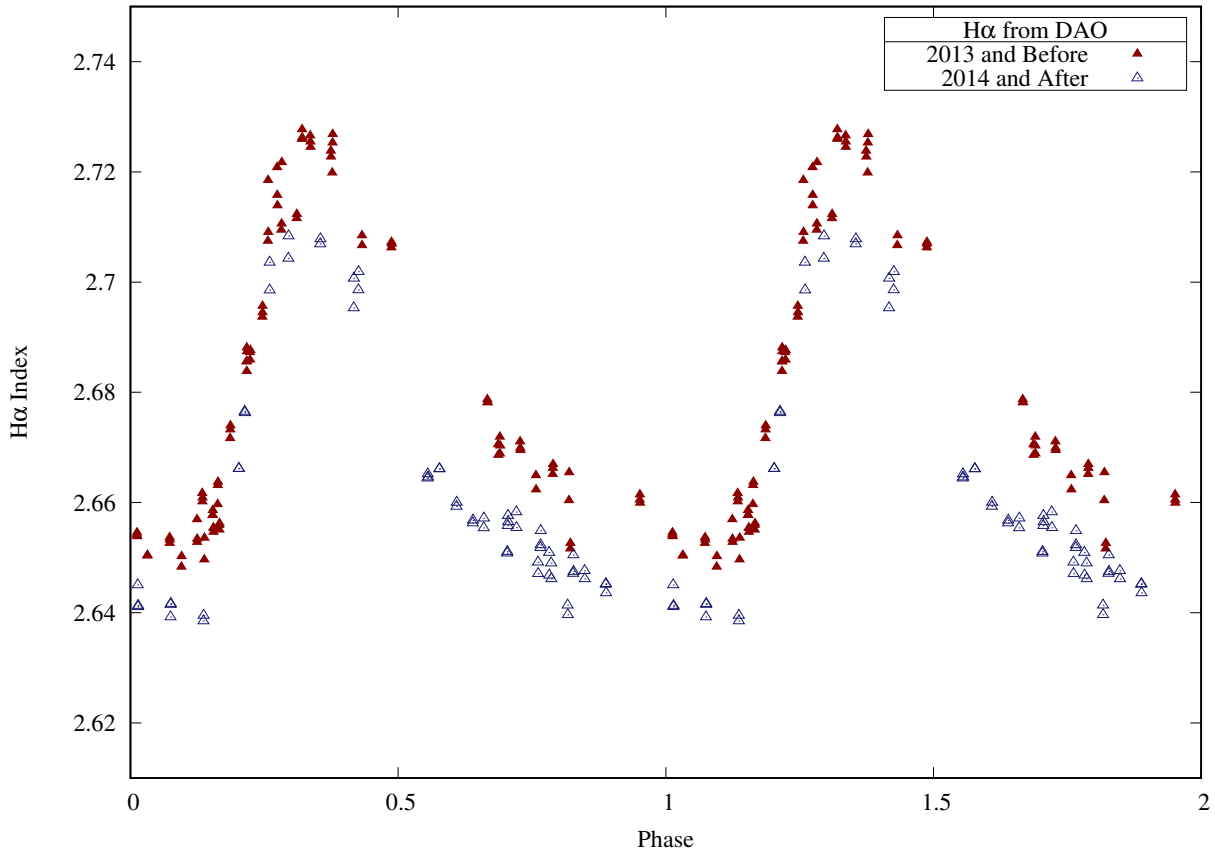

Figure 1.4 Temperature curves of X Cyg from spectroscopic observations at DAO. The Hα index was found by convolving the Hα filter response curves onto the spectra.

by using the filter set to take photometric measurements of the Hα spectral line. Second, we hoped to demonstrate the capacity of small telescopes to conduct serious astronomical research. The hope was that a small 8-inch telescope located in a polluted urban setting at BYU could reproduce the results a far larger and more expensive 1.2-meter telescope housed in a remote, professional observatory at DAO.

Chapter 2

Methods

2.1 System installation

In 2016 and early 2017, the observation deck on top of the Eyring Science Center was renovated to include permanent telescope piers. These piers include access points for power and data connections to BYU's computer network, providing a way for telescopes to be controlled from a computer. Soon decisions had to be made about what kinds of telescope systems to install and how to operate them.

Optical telescope systems for photometric work typically consist of several parts: the optical tube, containing the mirrors and/or lenses for light collection; a camera with a CCD and cooling system for taking data; a filter wheel for selecting and changing between filters; and a mount for pointing the system at targets and tracking them across the sky. Some telescopes also include dedicated guiders to help the mount keep a target centered in the frame. Others employ microfocusers that make small adjustments to keep images focused as well as possible. Further, large telescopes often are housed in a protective dome to prevent exposure to wind or rain, which can cause serious damage to sensitive and expensive equipment.

In addition to hardware requirements, robotic automation necessitates software to control the

system. The telescope must be able to automatically move to a target, change filters, take data, and move to another target. All this requires programmable software to communicate with the camera, filter wheel, and mount.

To decide which hardware and software components to use in this project, we considered both the project's goals and the cost of the systems. BYU already had several small unused telescopes on hand that were well-suited for scientific observation. The choice of mounts was based primarily off of the size of each optical tube—in general, the telescopes were small enough to use the smallest and least expensive mounts available.

The first robotic telescope system, photographed in Figure 2.1, uses a Vixen VMC200L 8-inch optical tube with an f/9.75 focal ratio. The camera chosen is a Finger Lakes Instrumentation MicroLine ML3200, with 2184 x 1472 pixel resolution and 6.8 μm pixel size, covering an area of the sky of about half of a degree. The telescope is pointed with a Software Bisque Paramount MYT telescope mount. We supply power to the mount, camera, and filter wheel from power outlets at the base of the telescope pier. Cables for the camera and filter wheel are threaded through the mount itself to prevent them from catching on the telescope as it maneuvers throughout an observing session. The optical tube is connected to the mount via a dovetail plate, held in place by screws. A notch was made in this plate to allow the cables to travel from the top of the mount to the instruments behind the optical tube. Data cables are connected to a USB hub attached to the pier; this hub then connects to the control computer via a CAT5 ethernet cable running under the deck floor.

Since the telescopes are located on the observation deck, exposed to the elements instead of inside a dome, they require some form of protection. At first, the telescope was protected with a tarp, and the camera and filter wheel were removed and brought inside at the end of each night. Later, we constructed a temporary cage from PVC pipe, fitted with a large tarp to shield the telescope from rain and wind. After several months a removable aluminum shed was constructed to house the telescope while not in use. This shed attaches to the telescope pier during the day and can be rolled

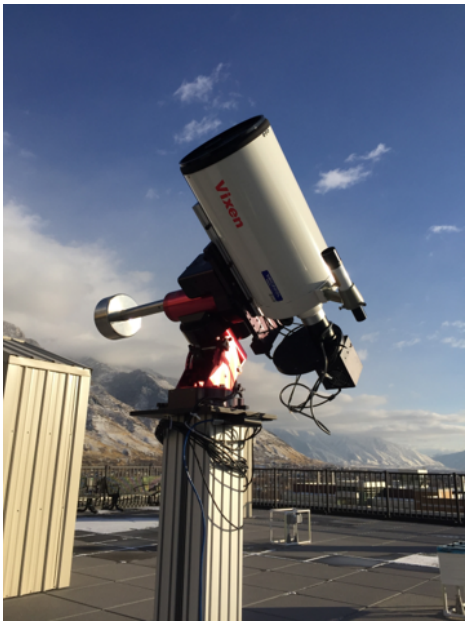

Figure 2.1 Photograph of the 8-inch robotic telescope on the observation deck of the Eyring Science Center.

aside before observation begins.

To control the system from a computer, we use a combination of three programs: TheSkyX , MaxIm DL , and CCDAutoPilot . TheSkyX is made by Software Bisque, the same company that produces the telescope mount we use. Its primary purpose is to find targets in the sky and point the telescope at them. Although TheSkyX is an incredibly versatile program, able to control not only the mount but also cameras, filters, and more, we found its capabilities for camera control lacking. Instead, we decided to use MaxIm DL to control the camera. MaxIm DL contains a package called PinPoint Astrometry, which provides a fast and efficient way to construct a plate solution, further explained in Section 2.6.1.

The final software component is needed to automate the system as a whole. The decision to use CCDAutoPilot for automation came after comparison with other options. The initial plan was to use the free program Orchestrate, also made by Software Bisque, but it was soon discovered that Orchestrate was incompatible with MaxIm DL . We briefly explored another program called CCD

Commander. However, CCD Commander makes it difficult to change observing plans each night. Each command must be input explicitly into a hard coded script. If a target needs to be added or removed, the individual commands dictating that target's part of the script must directly be edited. CCDAutoPilot, on the other hand, stores information for the observation run in a database and compiles all of that information together to form a script for each session. This structure makes it easy to activate or deactivate some targets, to change their order, or to change the number or kinds of observations for a target. Further, CCDAutoPilot can update a session with new information, even while it is running. This versatility, as well as its ability automatically to take high quality flat frames (cf. Sec. 2.4), proved an important factor in deciding upon its use.

2.2 Data collection

As with any other kind of observational work, measuring the Hα index required a list of targets that would be observable with our equipment and from our location. I created a target list by running a query through the Set of Identifications, Measurements and Bibliography for Astronomical Data (SIMBAD) database for Cepheid type variable stars with average magnitude in V less than 10. I then constrained the right ascension (RA) and declination (Dec) for the targets to areas of the sky that would be observable from Provo. Every few months, I ran the query again to acquire new targets as others fell out of observable positions. Table 2.1 shows a complete list of Cepheids studied.

Although not all targets are of the same variability type, the majority belong to three classes—Cep, DCep, and DCepS. The type Cep is a broad category of Cepheids, simply high luminosity, radially pulsating stars with long periods. The type DCep, on the other hand, indicates classical Cepheids, named after the prototypical Cepheid δ Cephei. Classical Cepheids are relatively young stars on the instability strip, often found in open clusters. DCepS types are classical Cepheids with small amplitudes and short periods. Included in the list are a few stars of other types. The Cep(B)

Table 2.1. Targets observed by the 8-inch telescope in 2017-2018. Unless otherwise noted, values are taken from the GCVS. The final three columns list the V magnitude at brightest, the average V magnitude, and the amplitude of oscillation in V magnitude. Sources are listed as superscripts, explained in the table comments.

Name	**RA** (h:m:s)	**Dec** (d:m:s)	**Type**	**Period** (days)	$\mathbf{V_{mag}}$ (brightest)	$\mathbf{V_{mag}}^{[\alpha]}$ (mean)	$\mathbf{V_{mag}}^{[\alpha]}$ (amplitude)
BG Lac	22 00 25.15	+43 26 43.3	DCep	5.331908	8.510	8.90	0.616
BQ Ser	18 36 15.94	+04 23 53.7	Cep(B)	4.2709	9.210	—	—
CD Cyg	20 04 26.56	+34 06 44.2	DCep	17.073967	8.350	9.01	1.180
EW Sct	18 37 51.11	-06 47 48.5	Cep(B)	—	7.770	—	—
FF Aql	18 58 14.75	+17 21 39.3	DCepS	4.470881	5.180	5.38	0.330
FM Aql	19 09 15.99	+10 33 08.9	DCep	6.11429	7.90	8.30	0.735
FN Aql	19 12 47.31	+03 33 26.7	DCepS	9.48164	8.110	8.40	0.556
GH Cyg	19 59 10.80	+29 27 02.7	DCep	7.81793	9.950	9.95	0.755
GY Sge	19 35 13.63	+19 12 08.6	DCep	51.0625	9.840	10.17	0.628
HD 122504$^{[\beta][\gamma]}$	14 01 57.76	+19 25 49.0	DCep	2.01	9.79	—	—
MW Cyg	20 12 22.83	+32 52 17.8	DCep	5.954586	9.140	9.51	0.720
RU Sct	18 41 56.38	-04 06 38.4	DCep	19.70062	8.820	9.53	1.120
SS Sct	18 43 43.51	-07 43 52.0	DCep	3.671253	7.900	8.23	0.510
SU Cyg	19 44 48.73	+29 15 52.9	DCep	3.8455473	6.440	6.89	0.755
SV Vul	19 51 30.91	+27 27 36.9	DCep	45.0121	6.720	7.28	1.080
SZ Aql	19 04 39.42	+01 18 22.2	DCep	17.141247	7.940	8.67	1.160
SZ Cyg	20 32 54.29	+46 36 04.6	DCep	15.10965	8.920	9.47	0.918
TT Aql	19 08 13.75	+01 17 55.2	DCep	13.754912	6.520	7.19	1.101
TYC 360-913-1$^{[\beta][\gamma]}$	15 47 42.95	+04 38 13.0	Cep	15.2	9.96	—	—
TYC 370-538-1$^{[\beta][\gamma]}$	16 07 04.28	+02 38 24.4	DCep	3.784	9.59	—	—
TYC 893-596-1$^{[\beta][\gamma]}$	13 42 24.92	+08 10 09.4	Cep	30.8	9.94	—	—
TYC 1033-3220-1$^{[\beta][\delta]}$	18 39 34.35	+11 22 52.6	DCep	1.152982	—	—	—
TYC 1488-210-1$^{[\beta][\gamma]}$	14 57 00.28	+17 58 16.1	Cep	0.95970	9.55	—	—
TYC 5064-1063-1$^{[\beta][\gamma]}$	17 05 08.50	-01 47 10.0	Cep	1.2775	9.40	—	—
TYC 5126-2068-1$^{[\beta]}$	18 47 41.16	-06 54 24.2	—	—	—	—	—
U Vul	19 36 37.73	+20 19 58.6	DCep	7.990676	6.730	7.15	0.724
V336 Aql	19 01 19.73	+00 08 49.3	DCep	7.30417	9.450	9.87	0.734
V473 Lyr	19 15 59.49	+27 55 34.7	DCepS	1.49078	5.990	—	—
V496 Aql	19 08 20.77	-07 26 15.9	DCepS	6.807148	7.560	7.76	0.373
V532 Cyg	21 20 32.9	+45 28 03.0	DCepS	3.283612	8.850	9.09	0.325

Table 2.1 (cont'd)

Name	**RA** (h:m:s)	**Dec** (d:m:s)	**Type**	**Period** (days)	$\mathbf{V_{mag}}$ (brightest)	$\mathbf{V_{mag}}^{[\alpha]}$ (mean)	$\mathbf{V_{mag}}^{[\alpha]}$ (amplitude)
V1154 Cyg	19 48 15.47	+43 07 37.0	Cep	4.925537	8.950	9.20	0.393
V1344 Aql	19 11 59.17	+04 21 17.5	DCepS	7.47693	7.620	7.77	0.288
V1359 Aql	20 03 39.97	-03 22 38.8	SRD	96.7	8.830	—	—
V1452 Aql	19 20 40.85	+14 25 08.8	Cep	2.3327	7.750	—	—
V1726 Cyg	21 29 38.94	+48 58 08.7	DCepS	4.2359	8.870	9.01	0.202
V2081 Cyg	19 27 48.95	+50 44 13.1	Cep	—	8.690	—	—
VZ Cyg	21 51 41.44	+43 08 02.5	DCep	4.864453	8.600	8.98	0.655
X Cyg	20 43 24.19	+35 35 16.1	DCep	16.386332	5.850	6.44	1.024
X Lac	22 49 03.18	+56 25 41.5	DCepS	5.44499	8.200	8.42	0.400
X Vul	19 57 28.61	+26 33 23.3	DCep	6.319588	8.330	8.88	0.779
Z Lac	22 40 52.15	+56 49 46.1	DCep	10.885613	7.880	8.45	0.964

$^{[\alpha]}$Magnitudes from Klagyivik & Szabados (2009)

$^{[\beta]}$RA and Dec from Gaia Collaboration (2018)

$^{[\gamma]}$Type, period, and V_{mag} from Schmidt et al. (2009)

$^{[\delta]}$Type and period from Berdnikov et al. (2009)

stars are Cepheids that simultaneously pulsate in more than one mode. V1359 Aql is an SRD star, a semiregular variable giant, sometimes classified as a Cepheid.

To obtain quality data, good observing practice must be followed. The lower a star is in the sky, the more the atmosphere obscures its light. As a general rule of thumb, any star below 30 degrees altitude is obscured enough to greatly reduce the quality of data. Thus, it is important to observe stars as close to the zenith as possible—above 30 degrees altitude unless absolutely necessary. To optimize the number of targets we could observe each night, I first roughly sorted the targets by RA, then checked what time each target rose and set at 30 degrees altitude, manually moving them in the order of which target set first. This way each target could be observed before it set too low in the sky, maximizing the number of targets each night.

In addition, proper exposure levels must be set for each target. Because the targets vary in magnitude, each needed to be observed individually to find a good exposure length in each filter. If an exposure length is too long, then too much light can enter the camera, overexposing the CCD; too short, and the signal can be muddled by noise (cf. Sec. 2.4). This sometimes proved problematic for the Hα filters, as the narrow filter is extremely opaque, so exposure lengths in different filters can vary greatly. For instance, some stars require exposures of only five seconds in the V filter, but five or ten minutes in the Hα filter. If a telescope system is known well enough, exposure levels for a given filter can be calculated based on a star's apparent magnitude. In our case, however, I set the exposures manually by moving to each target and experimenting with exposure lengths until achieving a decent photon count (usually between 10,000 and 30,000 photons at the peak pixel).

Over time, the telescope system gets knocked slightly out of alignment and must be readjusted to ensure proper tracking. Because of their reduced weight and stability, the smaller telescopes we use tend to lose their alignment more easily. Unfortunately this can cut into observing time, as fine alignment requires stars to be visible and usually takes several runs to achieve, often taking up hours or even a full night. In addition, weather also cuts into observable time considerably. Summer evenings, when most time was available to dedicate to research, often bring cloudy weather in Provo, which precludes any ability to take data.

The number of nights each target was observed and total number of observations in each filter are shown in Table 2.2. We observed some targets far more than others. BQ Ser, for instance, was observed on 28 nights, while some targets added only in 2018, such as V336 Aql, were only observed on two nights. We also made a critical mistake in our observations of V473 Lyr. At some point the sequence was unintentionally altered, and the narrow Hα filter was set to the Cousins R filter. Thus we ended up with massively overexposed images in R to accompany the wide filter exposures, losing about 10 nights of Hα measurements.

Table 2.2. Number of nights each target was observed, accompanied by the total number of observations in the V filter and Hα system.

Target	Nights Observed	V	Hα	Target	Nights Observed	V	Hα
BG Lac	8	10	10	TYC 1033-3220-1	26	39	34
BQ Ser	28	37	33	TYC 1488-210-1	2	2	2
CD Cyg	23	36	26	TYC 5064-1063-1	2	2	2
EW Sct	15	30	20	TYC 5126-2068-1	14	22	18
FF Aql	2	9	2	U Vul	23	36	26
FM Aql	25	37	28	V336 Aql	2	2	2
FN Aql	24	37	28	V473 Lyr	26	29	8*
GH Cyg	8	8	8	V496 Aql	16	31	19
GY Sge	2	2	2	V532 Cyg	14	23	19
HD 122504	2	2	2	V1154 Cyg	20	30	25
MW Cyg	17	31	21	V1344 Aql	10	26	14
RU Sct	24	32	28	V1359 Aql	10	23	14
SS Sct	14	26	19	V1452 Aql	24	37	28
SU Cyg	24	41	29	V1726 Cyg	15	23	20
SV Vul	24	37	28	V2081 Cyg	24	38	28
SZ Aql	25	40	28	VZ Cyg	21	30	27
SZ Cyg	25	39	29	X Cyg	26	122†	32
TT Aql	22	37	24	X Lac	19	28	25
TYC 360-913-1	2	2	2	X Vul	10	23	14
TYC 370-538-1	2	2	2	Z Lac	8	17	14
TYC 893-596-1	2	2	2				

*10 nights of data were accidentally taken in the R filter instead of the narrow Hα filter, unfortunately ruining a large portion of Hα measurements.

†The large number of observations is due mostly to 70 images in V being taken on the same night as part of initial testing of the system. I averaged every 10 observations when moving on to analysis. Another 11 images in V were taken the following night; these were averaged as well.

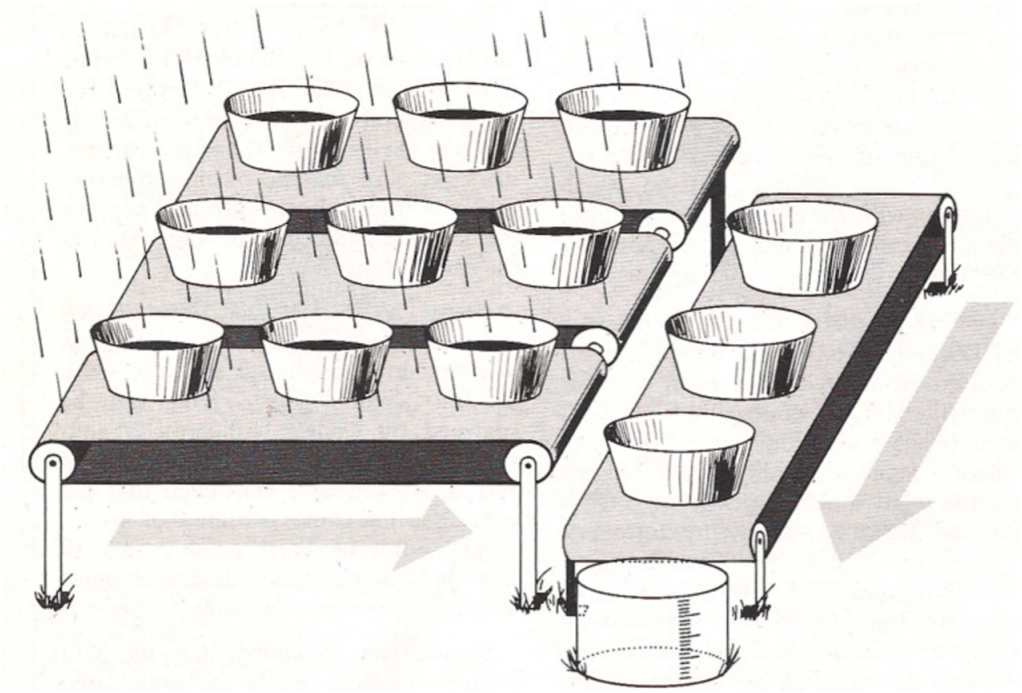

Figure 2.2 A CCD collects light much the same way as a system of buckets collecting rainwater. Each bucket dumps its water at the end of its row. Then all the water is moved downward and collected at a measuring station. Artwork by Steven Simpson, used with permission (Janesick & Blouke 1987).

2.3 CCDs

The device used by most astronomers to measure light is a charge-coupled device (CCD). A CCD is an array of electrodes, called pixels, made of a photosensitive material, usually silicon. As incoming photons strike the array, they generate free electrons through the photoelectric effect. Each pixel acts as a potential well for these electrons, effectively collecting charge in each well during the exposure. Once the exposure is finished, the voltages of the gates at the ends of each pixel are changed, shifting the electrons down each row, one column at a time. Then the same process is employed to shift the pixels in the readout column down to the output amplifier to be read, one pixel at a time. Once the entire column has been read, the next column is shifted over. This process continues until all electrons have been shifted to the readout column and then down to the output

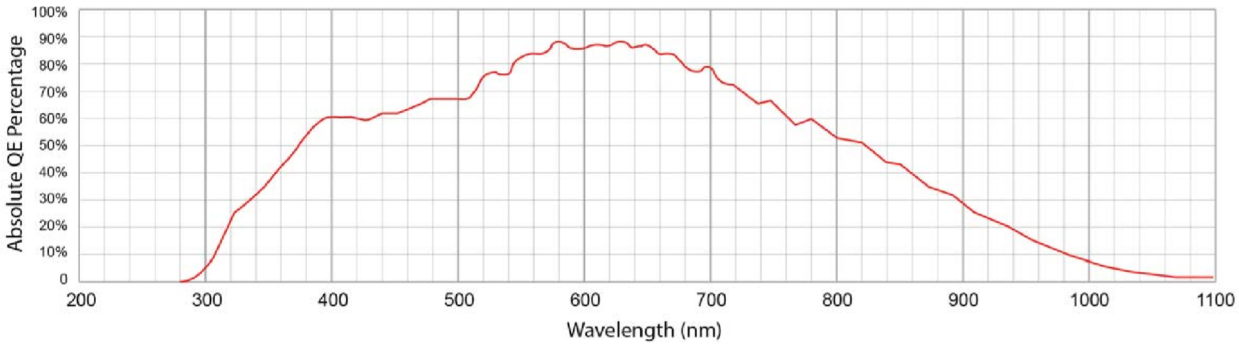

Figure 2.3 Quantum efficiency for the CCD used on the 8-inch telescope, from documentation provided by Finger Lakes Instrumentation.[1]

amplifier.

To aid understanding, a simplified version of the process is shown in Figure 2.2. Each pixel collecting photons can be thought of as a bucket collecting rainwater. Once the rain has stopped, the buckets are shifted over by conveyor belts until the buckets in the rightmost column have emptied into the lower level. Then, the newly-filled buckets are shifted downward into the measuring station, where the amount of water in each bucket is recorded. Once this is finished, the process is repeated until all the water has been measured—one column at a time is poured into the lower level, then each bucket in that lower level is poured into the measuring station.

Not every photon that strikes the CCD will create an electron, but the advantage of using CCDs is their extremely high quantum efficiency (QE). The human eye and photographic film detect only about 1% of photons that hit them; CCDs on the other hand can detect up to about 90%! The camera used for the 8-inch telescope uses an ON Semi KAF-3200ME CCD chip, whose quantum efficiency is shown in Figure 2.3. As the figure shows, this CCD collects photons most effectively at wavelengths between 400-800 nm, corresponding to the visible and very near infrared. Outside that range, it detects very few photons.

[1] http://www.flicamera.com/microline/index.html

2.4 Calibration frames

Images made from CCDs come with inherent noise that must be removed before analysis can begin. The three primary sources of noise are the bias level of the CCD, dark current from the exposure, and unevenness across the pixels of the chip. These sources of noise require different kinds of calibration images to be taken so that the noise can later be removed mathematically.

For the electronics of a CCD to work best, there must be an electric signal already in place across the chip. This electric signal is known as the bias level, typically resulting in roughly a thousand electron counts per pixel. Because these counts originate in the electronics themselves instead of an astronomical object, they must be removed. By taking an image without opening the shutter and reducing the exposure length as much as possible before reading off the chip, we can measure the bias level of the CCD. This kind of calibration frame is called a bias frame or zero frame, since the exposure length is effectively 0 seconds. Because the shutter is never opened, bias frames do not rely on any given light level and can be taken at any time during the day, as long as the CCD has cooled down to operating temperature. In practice, it is best to take calibration frames at the beginning or end of an observing session.

While an exposure is running, thermal energy from the silicon lattice of the CCD causes some electrons to be captured by pixels. The warmer the camera and longer the exposure, the more electrons get captured. The primary contributor to dark current is the temperature of the camera, so by cooling the CCD, we can get rid of most dark current. The ML3200 camera used in this project, for example, lists[2] a dark current at $-40°$ C of only 0.003 electrons/pixel/sec. However, in Provo, $-40°$C is too cold to consistently maintain. Instead, we operated between $-20°$C and $-30°$C, where dark current is substantially higher and must be removed. By taking another closed-shutter image, but with a longer exposure time, we can measure how much noise is introduced by dark current. These calibration frames, known as darks, include counts both from the bias level of the

[2] http://www.flicamera.com/microline/index.html

CCD and from the electrons introduced from dark current. Similarly to bias frames, darks can be taken at any time during the day since the shutter is closed, but are usually taken at the same time as bias frames. Prior to darks being taken, it is vital the CCD be cooled to the same temperature at which data are recorded. Although dark current theoretically scales linearly with exposure length, it is best practice to take darks with the same exposure length as the data that will be taken during an observing session to ensure the right number of counts is measured.

Finally, no matter how well a CCD is made, manufacturing introduces imperfections across the chip. Some pixels have higher quantum efficiency than others, producing higher counts from the same amount of light. Further, telescope optics are exposed to the elements and over time accumulate dust and debris. Even the smallest grains of dust on mirrors or filters get in the way and cause unevenness across the frame. If an exposure could be taken with a completely even amount of light hitting every pixel on the frame, then it could be determined which pixels are blocked by dust or which respond to light better than others. Such an image is called a flat frame. There are numerous ways to provide the light necessary take flat frames—some observatories illuminate the inside of the dome holding the telescope as a uniform light source; others use complicated systems of special reflective materials meant to distribute light as evenly as possible. Most observatories, however, simply use the sky.

Each pixel in a CCD has a maximum number of electrons that it can hold. After that number is reached, incoming photons are no longer detected; the pixel has been overexposed. In the camera we used for this project, the maximum counts per pixel is about 65,000. Since the goal of a flat frame is to measure the difference between pixel responses, the amount of light let into the camera during a flat frame cannot overexpose the pixels. In fact, after a certain number, the CCD no longer responds linearly to light, so measurements are no longer reliable. For our camera, any pixel with more than about 45,000 counts has been saturated too far and no longer provides an accurate measure of light. So flat frames should be taken with a light level bright enough to provide uniform illumination

across all pixels, but dim enough to prevent any pixels from reaching the point of nonlinearity.

The amount of light let into the camera can be controlled in two ways—by lengthening or shortening the exposure time of the flat frame, or by brightening or dimming the light source used. Because the camera uses a physical shutter to allow light in, any exposure less than about three seconds introduces unwanted shutter effects across the frame. Unfortunately the daytime sky is far too bright for even a three-second exposure, completely saturating the pixels. However, if flats are taken during twilight at dusk or dawn, then the sky will be at an appropriate light level. But this introduces an infuriating problem—as the sun sets or rises, the amount of light in the sky changes, so the exposure length for one flat may be too short or long for the next one! To maintain constant illumination, then, the exposure length must be continually adjusted for decreasing or increasing light. Further, since flats actually admit external light into the camera, they are filter-dependent. Not only can filters accumulate dust just as the telescope optics do, but they also allow different amounts of light through to the CCD. Thus acquiring quality flat frames becomes something of an art—a race against time before the opportunity is lost.

2.5 Data reduction

Many tools for applying calibration frames to data exist, but in this project I used the Image Reduction and Analysis Facility (IRAF). IRAF is a collection of software packages written mostly in the 1980s and used widely in astronomy both for data reduction and analysis. When observing, several calibration frames of each type are taken. Then various utilities in IRAF combine these frames and apply them. Note that the following procedure is standard only for optical photometry; spectroscopic work or photometry in other regimes require different methods to be employed.

The first step to calibrating data is to remove the bias level of the CCD. The *zerocombine* command in IRAF averages the counts in each pixel for all bias frames and produces a master bias

frame. Then, since the bias level is present on all images, this master bias frame is subtracted from all other frames—darks, flats, and data, usually using the *ccdproc* command.

Once the bias level has been removed, the next task is to remove dark current. Since the bias level has already been removed, the only source of counts still present on the dark frames is dark current. The *darkcombine* command acts similarly to *zerocombine*, averaging the counts in each pixel for all darks and creating a master dark frame. Then, the *ccdproc* command is used to subtract this master dark from all remaining images—flats and data. If the exposure length of the darks does not exactly match that of the flats and data, then the master dark must be scaled accordingly. For example, if dark frames were taken with an exposure length of 30 seconds, then a 2-minute object frame would require the dark to be scaled by 4 to ensure the proper amount of dark current is being subtracted off.

The application of flat frames is a bit more nuanced than that of bias frames or darks. While the bias level and dark current are simply extra counts that need to be subtracted, flat fields are meant to normalize the response of each pixel. Some "hot" pixels must have their counts reduced, while other "cold" pixels must have their counts increased. Just as in the previous two steps, the flats are combined using the *flatcombine* command, creating a master flat for each filter. This master flat is then applied to the object frames using the *ccdproc* command again, but the processing is more than just a simple subtraction. Each pixel value is divided by the average pixel count across the entire frame, normalizing the flat. So, "hot" pixels have normalized values higher than 1, while "cold" pixels have normalized values less than 1. When the flat is applied, each pixel in the object frame is divided by the normalized value for that pixel in the master flat, adjusting the photon count appropriately.

Other procedures are sometimes used to further calibrate data. CCDs often have bad pixels that simply do not work or even bad rows or columns that stop functioning. A bad pixel mask can be used to take these pixels into account. Often the edges of a CCD do not respond as well as the

center; these are sometimes removed by assigning a section to be trimmed during processing. While bad pixel masks and edge trimming were not employed in this project, they are common techniques.

Astronomical image files usually come in a Flexible Image Transport System (FITS) file format. These files include a header containing keywords and values associated to them providing fundamental information about the image. Headers include keywords denoting the type of image (e.g. object, bias), time an observation was made, target name, filter, and so on. Before an image is ready for analysis, its header must be complete. In particular, headers from the 8-inch telescope lack three fundamental values that must be calculated: sidereal time, Julian date, and airmass (a measure of how much atmosphere obscures the telescope's line of sight). The sidereal time is calculated and added to the headers directly by using the location of the observatory, the local time of observation, and the timezone. Then that sidereal time is used to calculate the Julian date and airmass through the *setjd* and *setairmass* commands.

2.6 Data analysis

Once the data were reduced using the methods explained in Section 2.5, analysis of the data could begin. Analysis included the following steps, detailed in the subsequent subsections: First, I performed plate solutions on any images that I could. Then, I measured the magnitudes of the Cepheids through single-aperture photometry and phased the results with their periods. Last, I performed differential photometry to obtain better results.

2.6.1 Plate solutions

Ideally, an object would appear in the same position every time a telescope pointed at it. In reality, no centering is perfect, so a target may change position from night to night. Additionally, a telescope's tracking across the sky to counteract the earth's rotation is imperfect as well, causing an object to

drift across the frame. As a result, no set pixel coordinate for a CCD can consistently represent the location of an astronomical target. This problem is addressed by performing a plate solution.

A plate solution maps each pixel in an image to a set RA and Dec coordinate in the sky. While a star moves across the sky over the course of a night, its RA and Dec coordinates remain fixed[3] and can be used to locate a star regardless of local time or position. When robotic telescopes center on a target, they slew to the target's coordinates, but they rarely center directly on the target. To compensate, a centering frame is taken and plate solution run to figure out how far off they are. The positions of stars are extracted from the image and compared with a massive database of star positions until a match is found. Then the telescope adjusts to center the target in the frame as best it can before taking data.

To perform a plate solution, RA and Dec must be transformed to a set of standard coordinates: ξ and η. Let A and D be the RA and Dec coordinates of the center of the image, and let α and δ be the RA and Dec coordinates of a given star on the frame. Then the standard coordinates for a star can be calculated by the equations (Hintz 2019):

$$\xi = \frac{\cos\delta \sin(\alpha - A)}{\sin D \sin\delta + \cos D \cos\delta \cos(\alpha - A)}$$
$$\eta = \frac{\cos D \sin\delta - \sin D \cos\delta \cos(\alpha - A)}{\sin D \sin\delta + \cos D \cos\delta \cos(\alpha - A)}. \tag{2.1}$$

Once these standard coordinates have been calculated for each star on the frame, they are then compared to the X (row) and Y (column) coordinates for the stars on the CCD using the equations (Hintz 2019):

[3]Stars do change position, but on timescales much longer than one night. Rather than constantly readjusting, stars' RA and Dec are catalogued every epoch of 50 years. The current epoch is J2000 and will be used until the year 2050.

$$\begin{aligned} \xi - X &= aX + bY + c \\ \eta - Y &= dX + eY + f, \end{aligned} \tag{2.2}$$

where the coefficients a–f are unknowns. In theory, these six unknowns can be solved with only three stars defining the plane; in practice, many stars are used, and a least squares regression is employed to find the most accurate fit. Once the coefficients have been determined, any X and Y position on the frame can be converted back to RA and Dec. First the X and Y coordinates are plugged into Equations 2.2 to determine that position's standard coordinates ξ and η, and then the position's RA (α) and Dec (δ) are determined through the equations (Hintz 2019):

$$\begin{aligned} \tan(\alpha - A) &= \frac{\xi}{\cos D - \eta \sin D} \\ \tan\delta &= \frac{\sin D + \eta \cos D}{\cos D - \eta \sin D} \cos(\alpha - A). \end{aligned} \tag{2.3}$$

I used three different methods to perform plate solutions. TheSkyX includes a software package called Image Link that can analyze an image and compare it to either a local or online database. CCDAutoPilot is able to utilize this part of TheSkyX to perform plate solutions as data are taken and input the information into the file headers. By 2018, I had configured the settings in the two programs properly, allowing for consistent automatic plate solving during data collection. However, not all frames were able to plate solve correctly. The data taken in 2017 was mostly unsolved, as were some frames from 2018 that either did not have enough stars in the frame or otherwise failed to meet some parameter for plate solution.

To solve these frames, I primarily used the PinPoint Astrometry package contained within MaxIm DL. Due to licensing issues, PinPoint cannot be controlled remotely through another program such as CCDAutoPilot , but must be used directly by the user. This means each individual

file must be opened and run through PinPoint to perform the plate solution. Though this seems at first tedious, PinPoint is remarkably fast at its job, usually completing a plate solution in only a second or two. Thus a relatively large data set can be manually solved this way without too much hindrance.

For those frames which were unable to be solved by the previous two methods, I used one final option—uploading the images to astrometry.net. Uploading images to an online database is decidedly slow, taking several minutes to solve each frame. However, it offers the most robust method, often able to complete a solution when other methods fail. Occasionally, even astrometry.net was unable to solve a frame; some images (particularly those taken in the narrow Hα filter) simply had too few stars to produce a reliable plate solution. When this happened, I considered the frame unsolvable and made a note to measure it manually.

Creating plate solutions whenever possible ensured that the computer could locate stars on any frame, regardless of how they may have shifted. Then, the process of calculating magnitudes using photometry (cf. Secs. 2.6.2, 2.6.3) was far quicker and more efficient; all plate-solved images of a target could be measured at the same time.

2.6.2 Aperture photometry

Although stars can often be thought of as point sources of light, their light spreads out across several pixels, creating a Point Spread Function (PSF) similar to a Gaussian profile. Thus, their light output cannot be measured at any specific pixel, but rather must be counted as the PSF falls off. The actual measurement of photons involves placing an aperture around a star's position on a frame and adding the total number of photons from each pixel inside of the aperture. The width of the aperture can vary, but generally a diameter of 1.5 multiplied by the full-width half-max (FWHM) of the PSF provides a good amount of signal without introducing too much background noise. For pixels that are cut across by the aperture, a fraction of the photons corresponding to the area enclosed

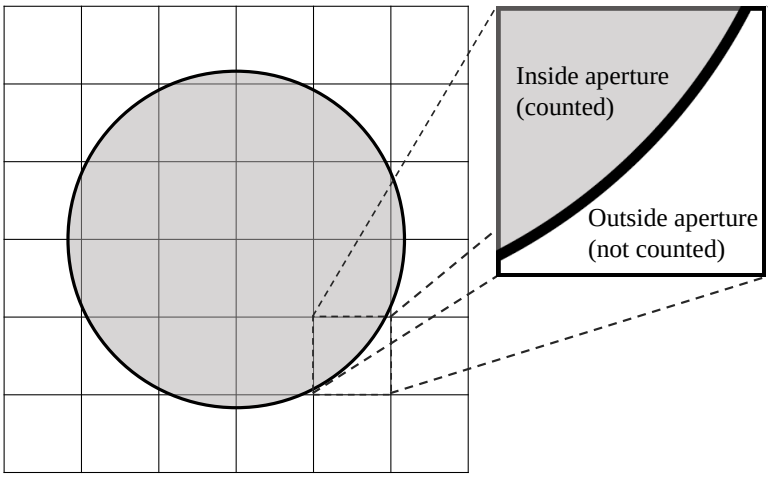

Figure 2.4 Example of aperture bisecting a pixel. Only a fraction of the photons in the pixel are counted.

is counted rather than the entire well (cf. Fig. 2.4). However, this number includes not only the photons that come from the star, but also background photons emitted by the sky itself. These background counts must be subtracted from the aperture counts to give a proper measure of the star's output.

To measure the background, two additional annuli separate from the aperture are placed farther away from the star, where the star's radial profile has reduced to the background noise. Then, the counts from pixels between these annuli are added together to measure the output of the sky. The counts are then averaged to remove the effects of any stars that may have been located between the annuli. Figure 2.5 shows a typical radial profile of a star's PSF. Vertical lines indicate PSF's FWHM and the radii at which the aperture and sky annuli are usually placed.

Once the average sky noise per pixel has been determined, it is multiplied by the number of pixels located within the aperture and subtracted from the target counts. This finally produces a measurement of a star's apparent brightness—flux, in units of counts/sec. Flux can then be converted into magnitudes using

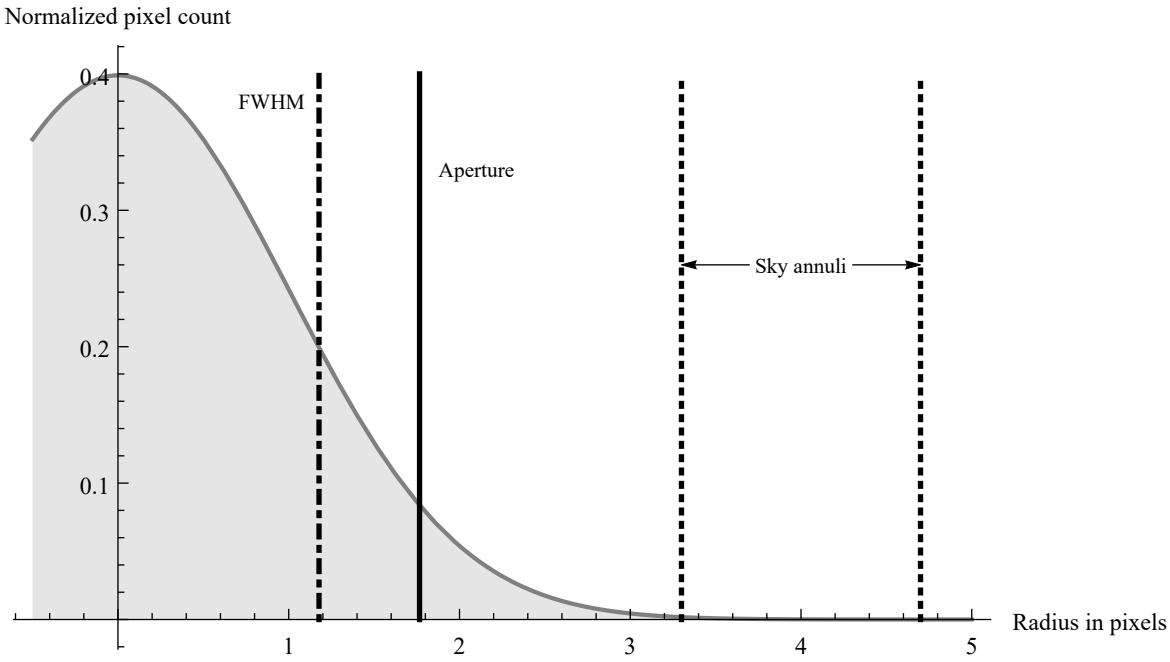

Figure 2.5 Typical radial profile of a star, following a Gaussian distribution. Vertical lines represent the radii of the FWHM, aperture, and sky annuli.

$$m = -2.5\log_{10}(f) + z, \tag{2.4}$$

where m is magnitude, f is flux, and z is an arbitrary zeropoint. Note that these calculated magnitudes are only apparent instrumental magnitudes; conversion to absolute magnitude requires correction for airmass and comparison to well-known standard stars.

Although many programs for conducting aperture photometry exist, such as AstroImageJ (Collins et al. 2017), in this project I used the *phot* package within IRAF. The *phot* package computes magnitudes through a complicated algorithm including many user-set and data-dependent parameters, beyond the scope of this paper. To use *phot*, IRAF requires a file listing the coordinates of any apertures to be placed for measurement. I created this coordinate file by opening a plate solved image in SAOImageDS9[4], an image display program integrated into IRAF, and selecting

[4] http://ds9.si.edu/site/Home.html

the location of the star on the frame. Naturally, each target requires a different coordinate file, but because the images are plate solved, one coordinate file translates across all images of a target. For the few frames which could not be plate solved, I manually set image X and Y coordinates for *phot*.

The *phot* package outputs its measurements into *.mag* files, containing detailed statistical information about how magnitudes are measured. From these files I extracted the image file name, time of observation, filter, magnitude, and observational error. I then compared observations taken on the same night and subtracted the wide Hα magnitudes from the narrow Hα magnitudes to arrive at the sought after result: an index measuring the strength of the Hα line. Using periods taken from the literature (cf. Table 2.1), I then determined at which point in the star's pulsation cycle each observation was taken, using the first image as the start of the cycle. By phasing the data this way, I could combine observations taken over long periods of time. Finally, I plotted the Hα indices and magnitudes in V against the phase of each observation (in the case of Hα, observation time was averaged between the narrow and wide filters).

2.6.3 Differential photometry

In practice, a single aperture is an imperfect way to take a scientific measurement. Differences in seeing from exposure to exposure change the amount of light gathered, artificially introducing scattering to the data. As discussed below in Section 3.1, the quality of light curves using magnitudes from IRAF's *phot* command were poor. To mitigate the problem of changes in seeing and improve the quality of light curves, I employed the technique of differential photometry.

Rather than placing a single aperture only around the target star, differential photometry involves placing apertures around other comparison stars, presumed to be constant. The brightness of the target star is then compared to the ensemble of comparison stars, producing measurements of relative magnitudes. To perform differential photometry, I uploaded reduced images to VPhot[5] and

[5] https://www.aavso.org/vphot

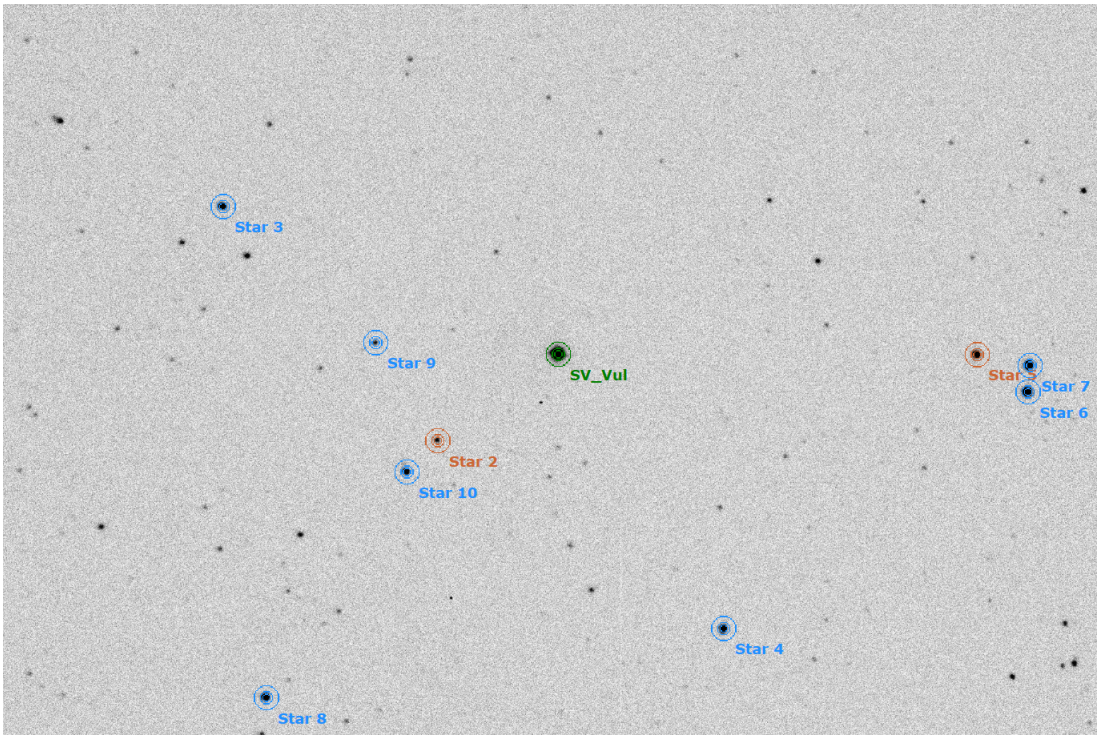

Figure 2.6 Ensemble used for differential photometry of SV Vul using VPhot. The blue apertures surround comparison stars in the ensemble; the red apertures (stars 2 and 5) surround check stars, used to ensure the ensemble remains constant and is not variable.

created ensembles of comparison stars for each target. Figure 2.6 shows an example of an ensemble used for differential photometry. The target star, SV Vul, is centered in the frame, surrounded by a green aperture. Blue apertures surround the comparison stars constituting the ensemble, while red apertures surround check stars (2 and 5) used in Vphot to ensure the ensemble remains constant.

Differential photometry in general produces higher quality light curves than a single aperture. However, it brings with it its own challenges. For example, good comparison stars ought to be of roughly the same brightness as the target star, but this is not always possible. Sometimes a target may be far brighter than any nearby stars in the frame. This presented a particular challenge for dimmer targets—especially in the narrow Hα filter. Some stars' ensembles consisted of only two or three stars, and these comparison stars often were decidedly fainter than the target. Additionally, the subtraction of measurements in the two Hα filters requires that the ensembles for the two filters

be the same, even though one exposure may have much higher signal-to-noise than the other. Thus comparison stars used for the wide filter may be almost undetectable in the narrow. To prevent this from causing problems, I used images taken in the narrow filter to place comparison stars; this reduced the number of stars in the ensemble, but it ensured that the stars would be detected in all frames.

Once the differential magnitudes were calculated in VPhot, I used Period04 to phase the data with the aforementioned periods (cf. Table 2.1). I then duplicated this phased data to lengthen the curves to a phase of 2. Duplicating the data in this way helps to show all parts of the light curve, irrespective of where in the star's cycle the phased plot begins. I present the results of this work, the phased differential light curves for a selection of Cepheids, in Section 3.1.

2.7 Determining periods

As shown in Table 2.1, not all targets had periods listed in SIMBAD. I attempted to determine periods for these objects using Least-Squares Spectral Analysis (LSSA). Sometimes called the Lomb-Scargle method after Nicolas Lomb and Jeffrey Scargle, who contributed to the method's development, LSSA is similar to Fourier analysis, but helps to reduce noise when data have large gaps between points. The exact mathematics governing the Lomb-Scargle method is beyond the scope of this paper, but it is an effective and robust technique for determining likely periods from a set of data.

I used the program Peranso to create Lomb-Scargle periodograms for the targets in the study with unlisted periods, namely EW Sct and V2081 Cyg. I also examined TYC 1033-3220-1 and V1452 Aql, whose periods produced poor light curves when the data were phased. I ran the Lomb-Scargle method for a range of periods between 1.1 days and 45 days, since that range would capture most Cepheids. I then examined phased plots of the data using the most likely periods from the analysis

to see how well they reproduced light curves.

One limiting factor of Peranso is that combining data sets is difficult—the difference in offset when instrumental magnitudes are calculated can cause one data set to appear much brighter than another. This proved troublesome for EW Sct and V2081 Cyg, for which I combined observations taken at BYU with the 8-inch telescope with archival data from the American Association of Variable Star Observers (AAVSO). (By increasing the number of observations used in the Lomb-Scargle analysis, I hoped to more precisely identify the most likely period of oscillation.) To overcome this problem, I used Period04 instead of Peranso. Period04 makes it more difficult to isolate more than one likely period, but it makes combining data sets much easier, as it normalizes each set to its mean value. I discuss the results of period analysis in Section 3.2.

Chapter 3

Results & Conclusions

3.1 Quality of light curves

Single-aperture photometry in IRAF yielded poor results. Figure 3.1 shows single-aperture light curves for two of the Cepheids, X Cyg and CD Cyg. Once phased, clear light curves should have emerged, at least in the V filter, where the S/N is the highest. Of the curves in the figure, however, only the V curve for X Cyg presents any clear evidence of regular pulsation. Most of the other Cepheids showed only extremely poor light curves or no pattern at all. Different levels of seeing on each night due to airmass, clouds, or other effects likely interfered with the precision of our measurements. In addition, the narrow Hα filter is so opaque that obtaining a decent S/N was impossible for some of the Cepheids. Because of this, we decided to take mulit-aperture differential measurements, described in section 2.6.3. The quality of the differential light curves was superior to the single-aperture measurements.

In the following subsections I present the light curves for 16 of the 41 Cepheids studied. Most of the Cepheids presented show good curves in the wide Hα filter and in V. The narrow Hα filter, however, usually created too much scatter to obtain reliable Hα indices. In each case, the Hα index

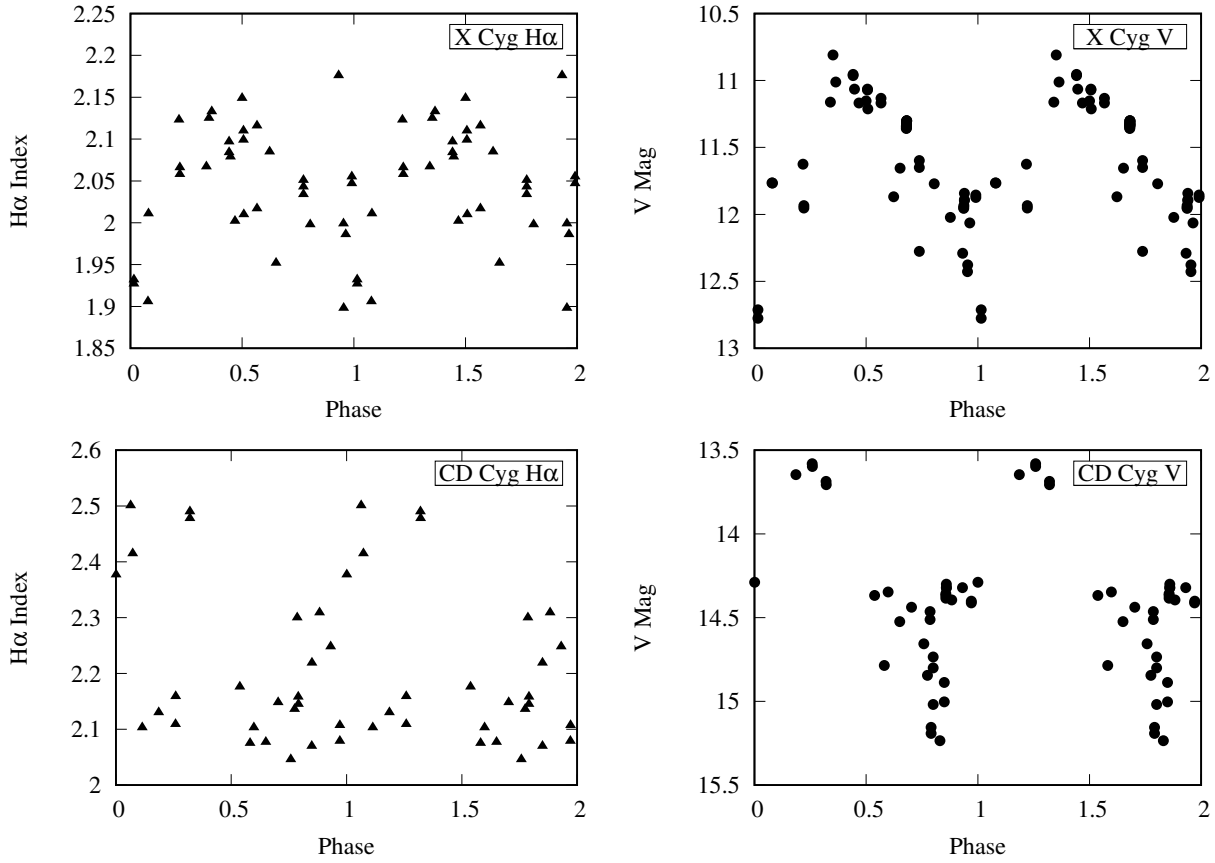

Figure 3.1 Single-aperture light curves of X Cyg and CD Cyg in the Hα index and in V. While the curve in V for X Cyg shows clear pulsation, the trend in CD Cyg is far less defined. Likewise in Hα, X Cyg shows some mild signs of pulsation, but CD Cyg shows no clear pattern. These results were later improved by conducting differential photometry (cf. Secs. 3.1.2 and 3.1.15).

curve was phased separately from each filter, so observations at a given phase do not necessarily correspond to the same phase in the Hα filter curves. Error bars are shown only when they are large enough to differentiate from the point markers on the curves themselves.

3.1.1 BQ Ser

BQ Ser is a Cep(B) type, a multimodal Cepheid. Thus phasing it with only one period produces an untidy light curve. Even the differential light curve in V (cf. Fig. 3.2) is somewhat messy.

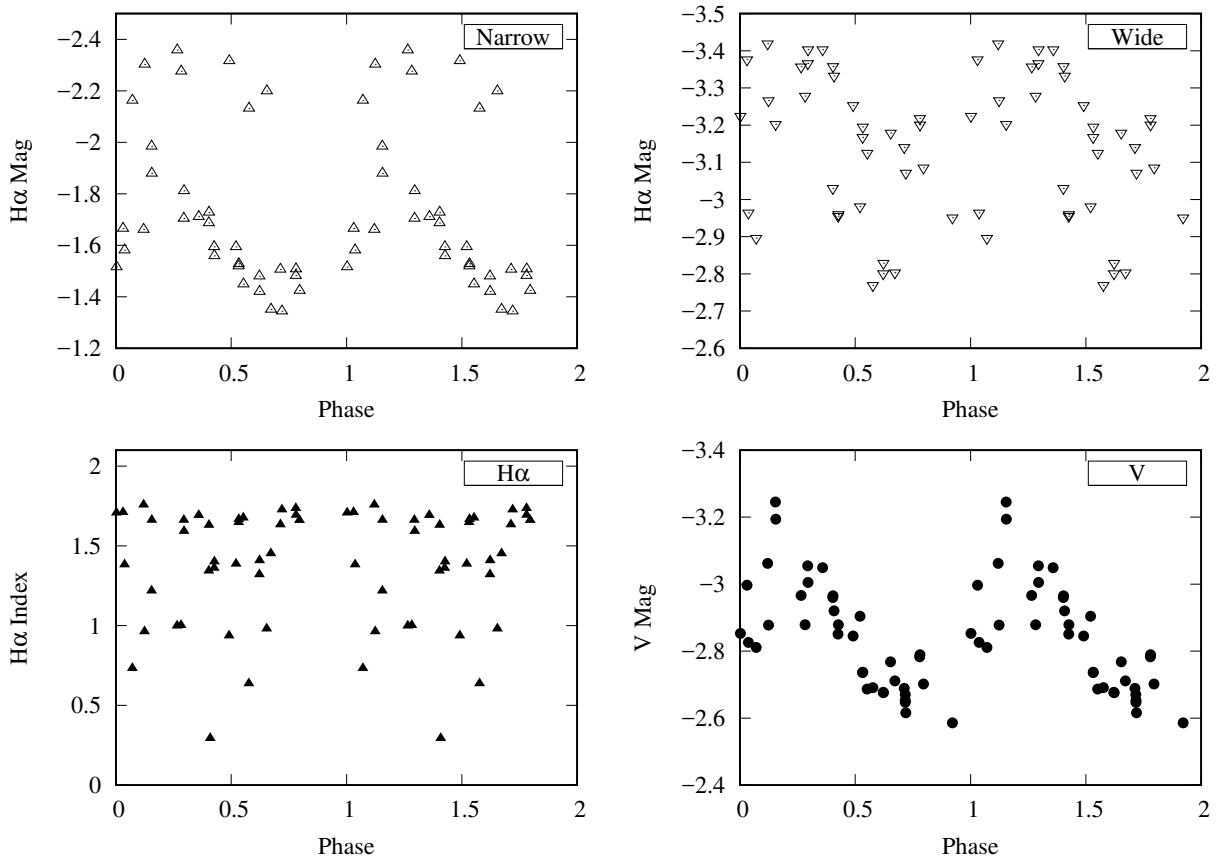

Figure 3.2 Differential light curves of BQ Ser

Further, the curves in both the wide and narrow Hα filters show little pattern. A curve in the narrow can be readily observed, but too many bad points disrupt the pattern. In the end, the Hα index measurements show little promise.

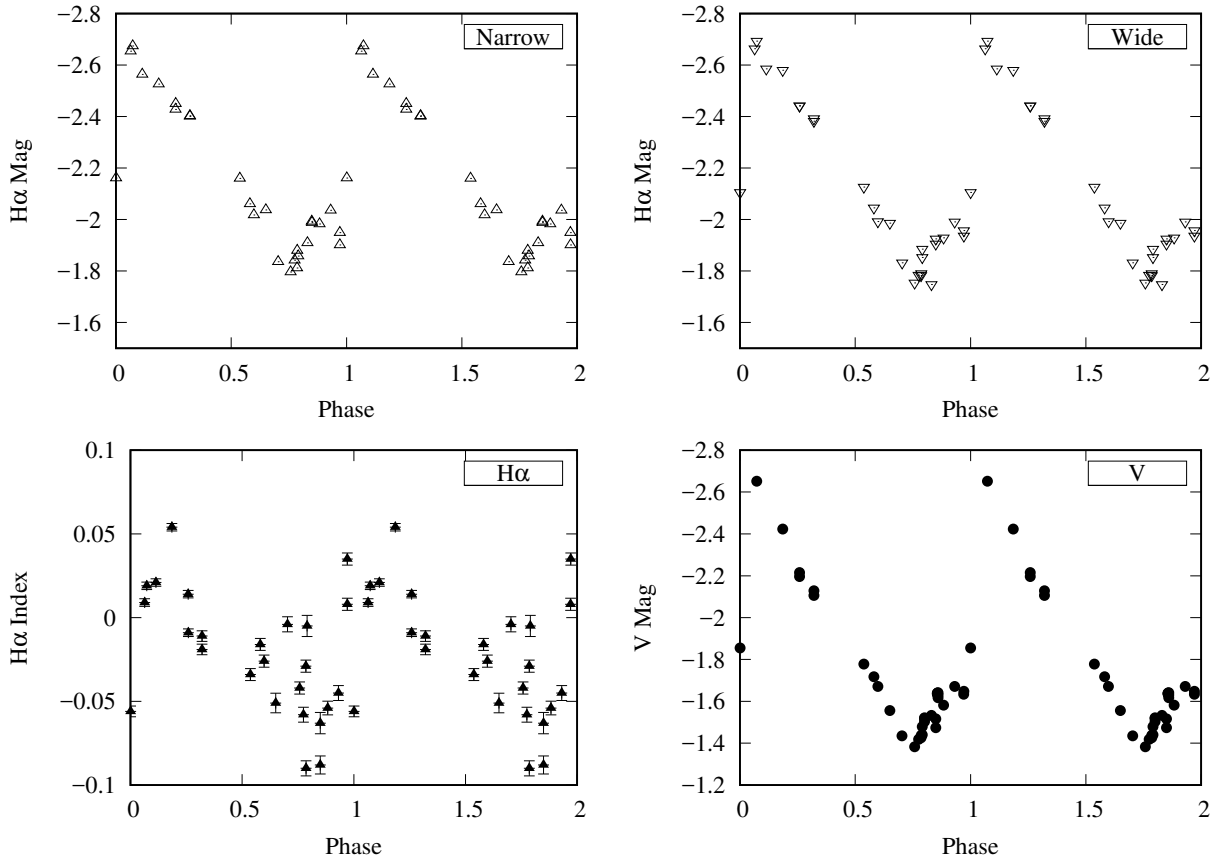

Figure 3.3 Differential light curves of CD Cyg

3.1.2 CD Cyg

CD Cyg shows very clear differential curves in all three filters (cf. Fig. 3.3). However, the Hα indices show only small oscillations—small enough that statistical errors in measurement may change the shape of the Hα temperature curve. Still, although it is nowhere near as sharply defined as in each individual filter, there appears to be a clear indication of some regular oscillation in the Hα index.

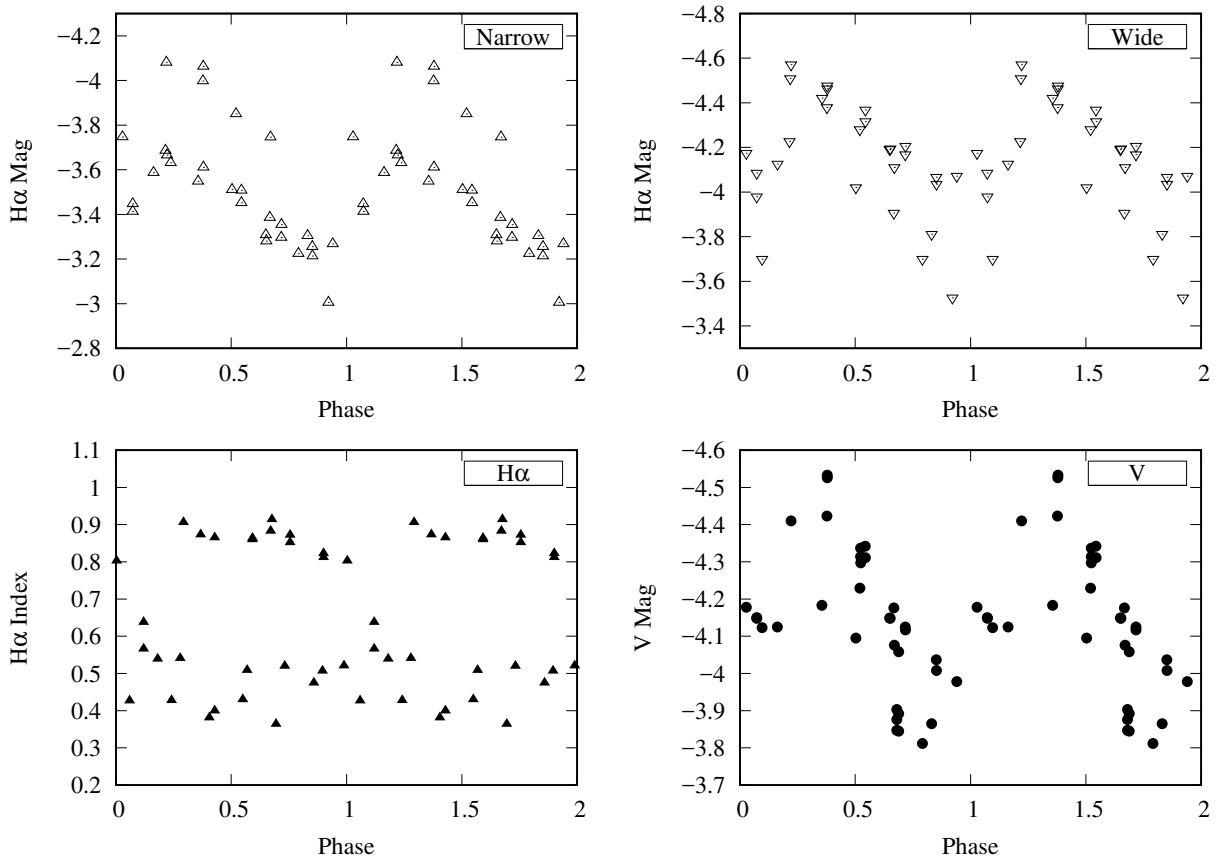

Figure 3.4 Differential light curves of FM Aql

3.1.3 FM Aql

The apparent presence of second curves in the narrow and wide filters (cf. Fig. 3.4) at first indicated the possibility of a temperature shift in FM Aql between 2017 and 2018. Upon closer inspection, the high magnitudes in the narrow and low magnitudes in the wide occurred in both 2017 and 2018, precluding the possibility that FM Aql experienced something akin to X Cyg's temperature drop. That said, the two seemingly discrete ranges for Hα is curious and certainly merits further inspection.

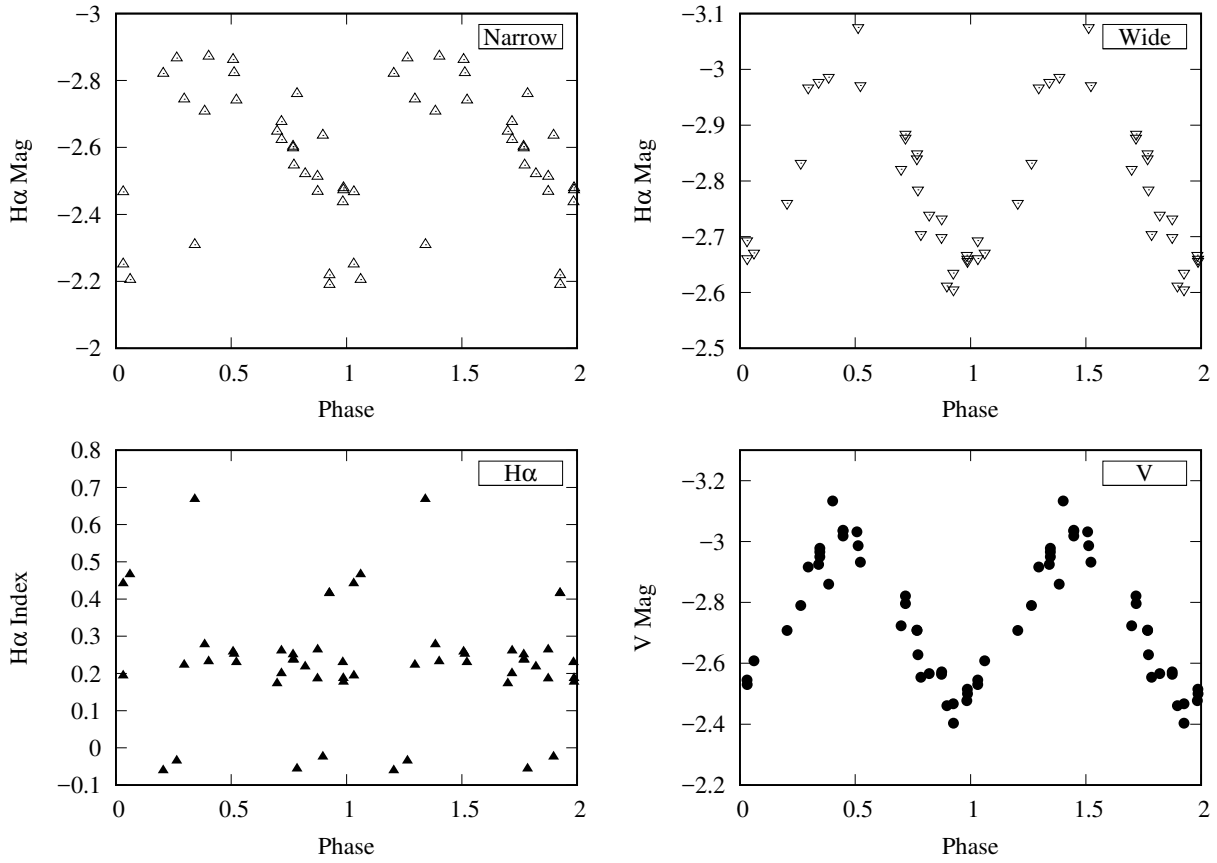

Figure 3.5 Differential light curves of FN Aql

3.1.4 FN Aql

FN Aql suffered heavily from poor S/N in the narrow filter. The differential measurements in the wide filter and in V (cf. Fig. 3.5) show clear light curves, but the narrow filter's measurements are unfortunately muddled. The result then is that the Hα measurements show no clear significant pattern. The presence of repeated measurements of low Hα index are almost certainly simply an artefact of poor measurements in the narrow filter.

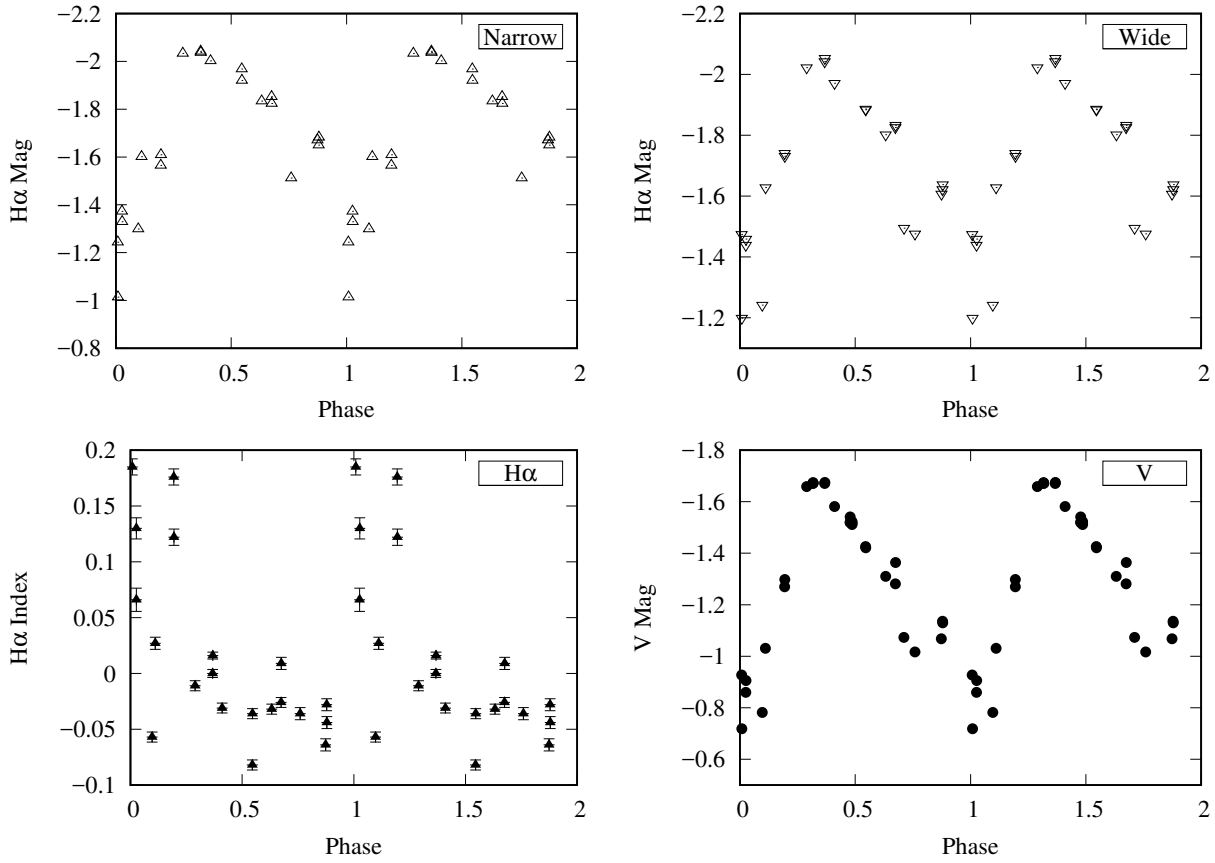

Figure 3.6 Differential light curves of MW Cyg

3.1.5 MW Cyg

MW Cyg's differental curves (cf. Fig. 3.6) show clear curves in both Hα filters and in V. Similarly to CD Cyg, however, the magnitudes for the narrow and wide filters are similar enough that statistical error could change the shape of the Hα curve. There appears to be some oscillatory nature to Hα, but low S/N in the narrow filter likely disturbs the curve.

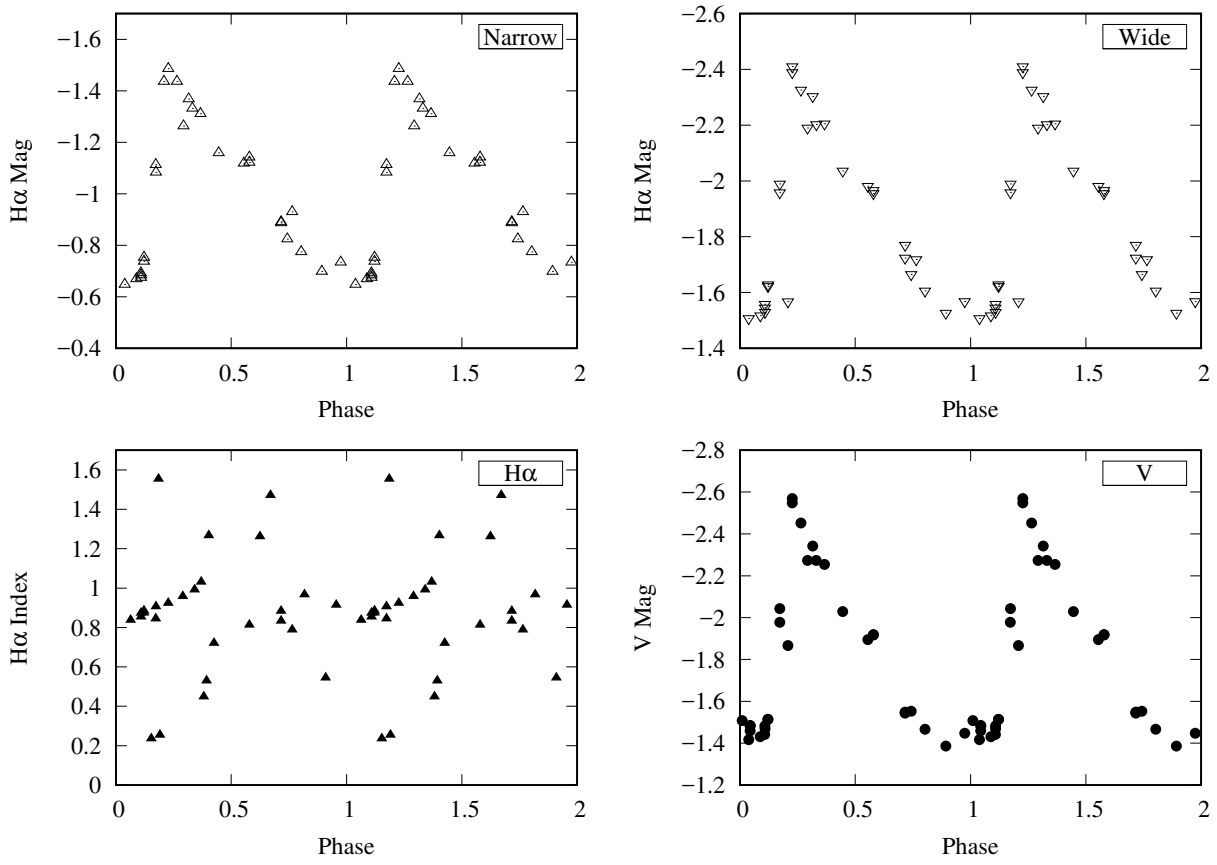

Figure 3.7 Differential light curves of RU Sct

3.1.6 RU Sct

RU Sct shows clear, distinct differential light curves in all three filters (cf. Fig. 3.7). In light of this, the lack of any clear pattern in Hα curve is surprising—the amount of scatter is much larger than expected. Curiously, Hα seems to track fairly consistently up to a phase of about 0.4, after which the pattern dissolves. Whether this is indicative of any actual tracking of temperature is unclear and warrants further analysis.

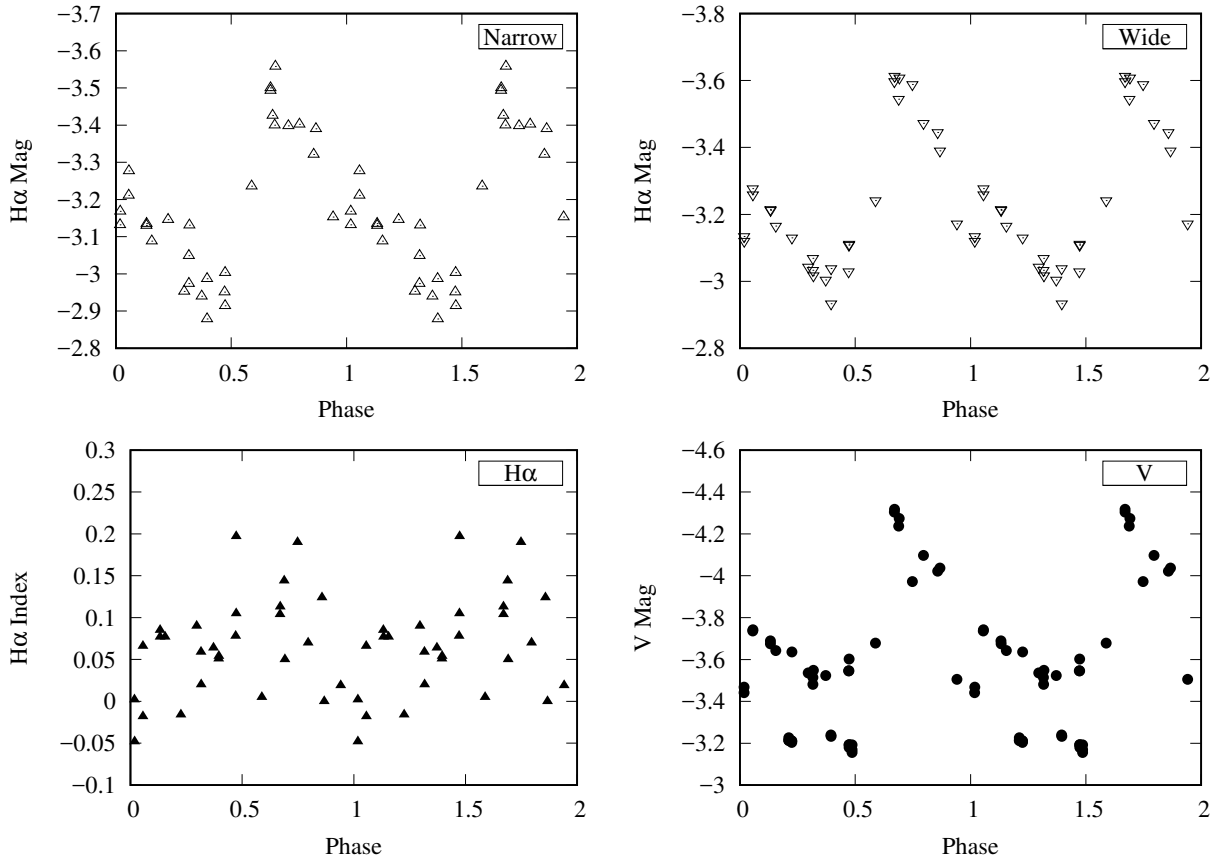

Figure 3.8 Differential light curves of SU Cyg

3.1.7 SU Cyg

Deviating from the rest, Su Cyg shows clearer differential curves in the Hα filters than in V (cf. Fig. 3.8). This is most likely due to poor seeing on a few nights in 2017, as initial observations with the 8-inch telescope were made in V without Hα. Though the trend is weak, there appears to be an indication of regular oscillation in the Hα index curve. Thus SU Cyg's temperature may be tracking, albeit with large scatter in the data.

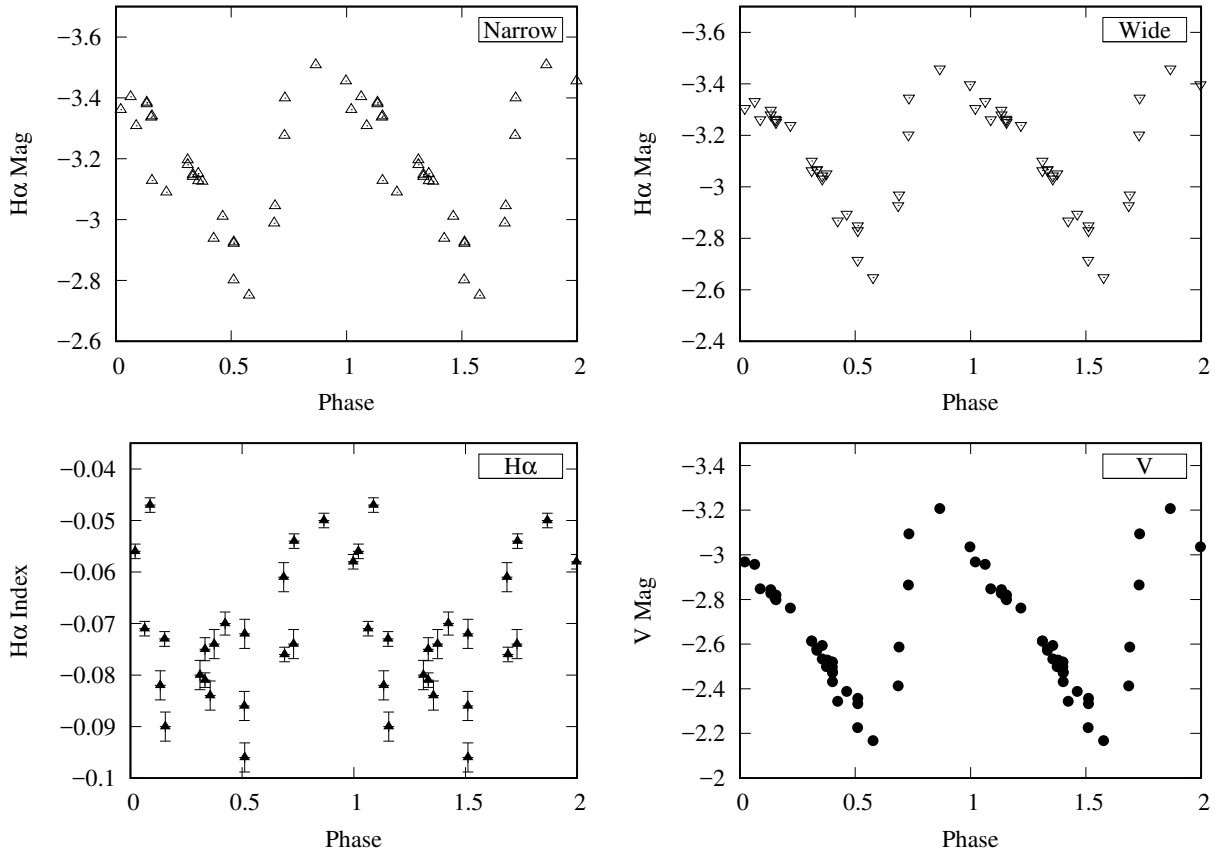

Figure 3.9 Differential light curves of SV Vul

3.1.8 SV Vul

Similarly to SU Cyg, SV Vul shows clean differential curves in all three filters (cf. Fig. 3.9). In addition, the Hα index curve, while somewhat scattered, clearly indicates regular oscillation. The Hα index may be properly tracking the temperature curve in this case. The small amplitude of oscillation in Hα is nevertheless concerning. Observational error could considerably alter the shape of the curve.

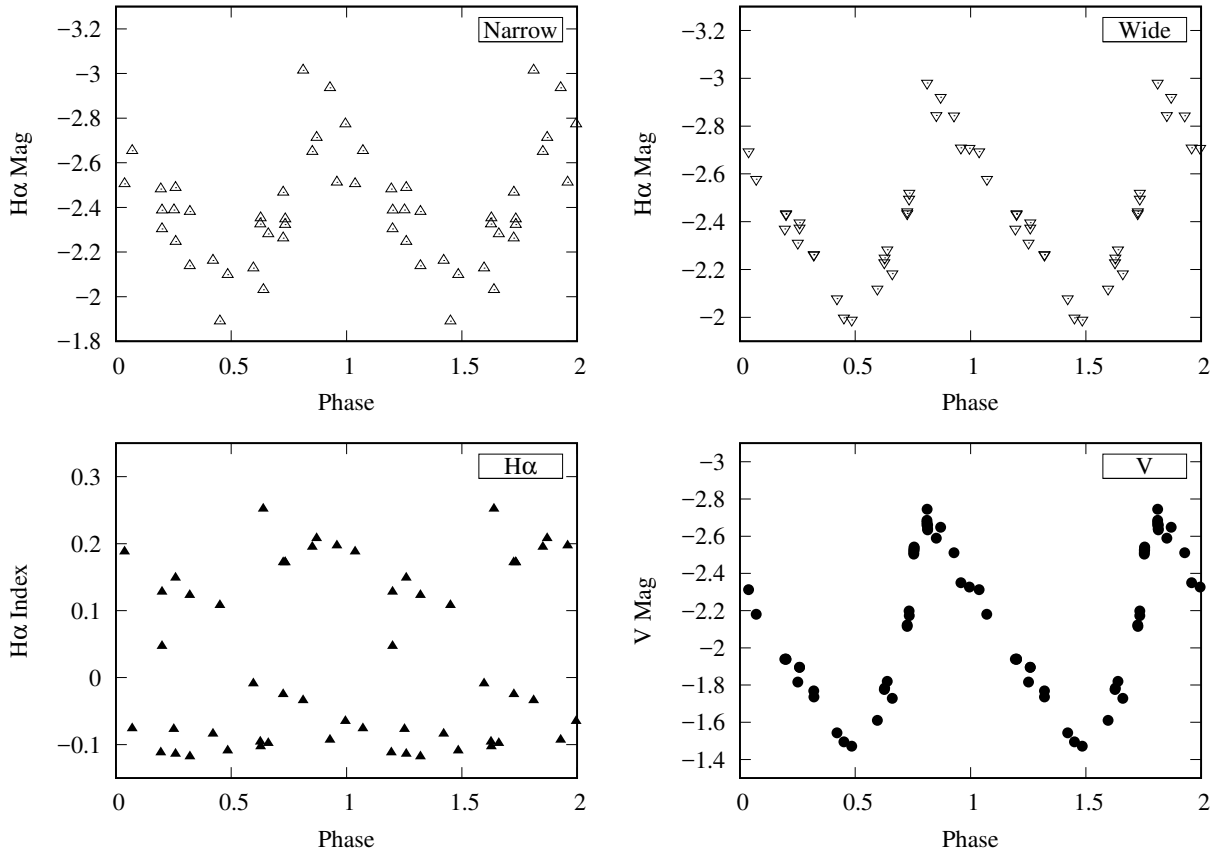

Figure 3.10 Differential light curves of SZ Aql

3.1.9 SZ Aql

The differential measurements for SZ Aql show clearly defined curves in all three filters (cf. Fig. 3.10). However, the large scatter in the narrow filter confuses the Hα index curve, eliminating any steady temperature tracking. Similarly to FM Aql, the two seemingly discrete ranges for Hα index raised the possibility that SZ Aql may have undergone a temperature shift. Upon closer inspection, however, values from both apparent ranges occur in both 2017 and 2018. The scatter is likely simply the result of poor seeing on some nights, which affects the narrow filter more than the others.

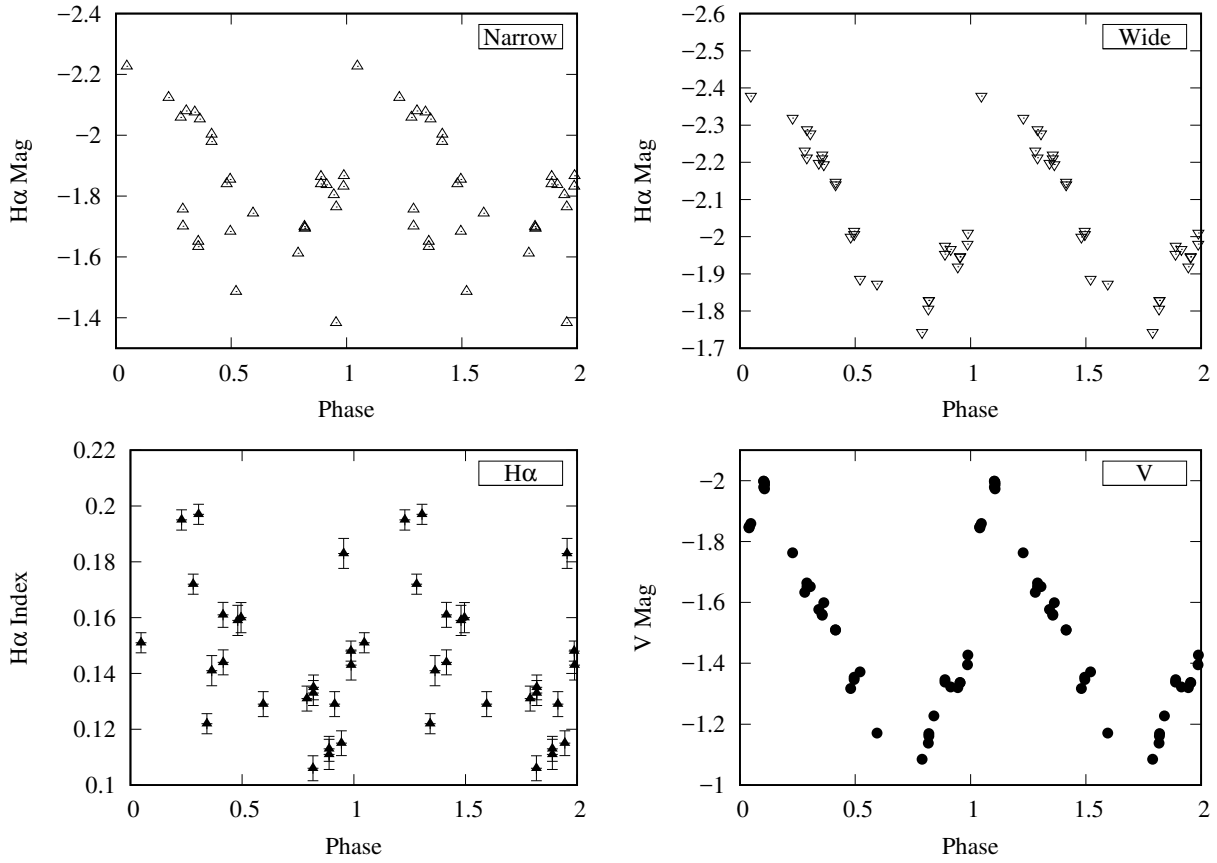

Figure 3.11 Differential light curves of SZ Cyg

3.1.10 SZ Cyg

Poor S/N heavily obscured narrow filter data for SZ Cyg (cf. Fig. 3.11). While the wide filter and V filter each show well-defined curves, the narrow filter creates too much scatter in the final Hα index curve. Further, the magnitudes of the narrow and wide filters were similar enough that statistical error alone could significantly alter the shape of the Hα index curve.

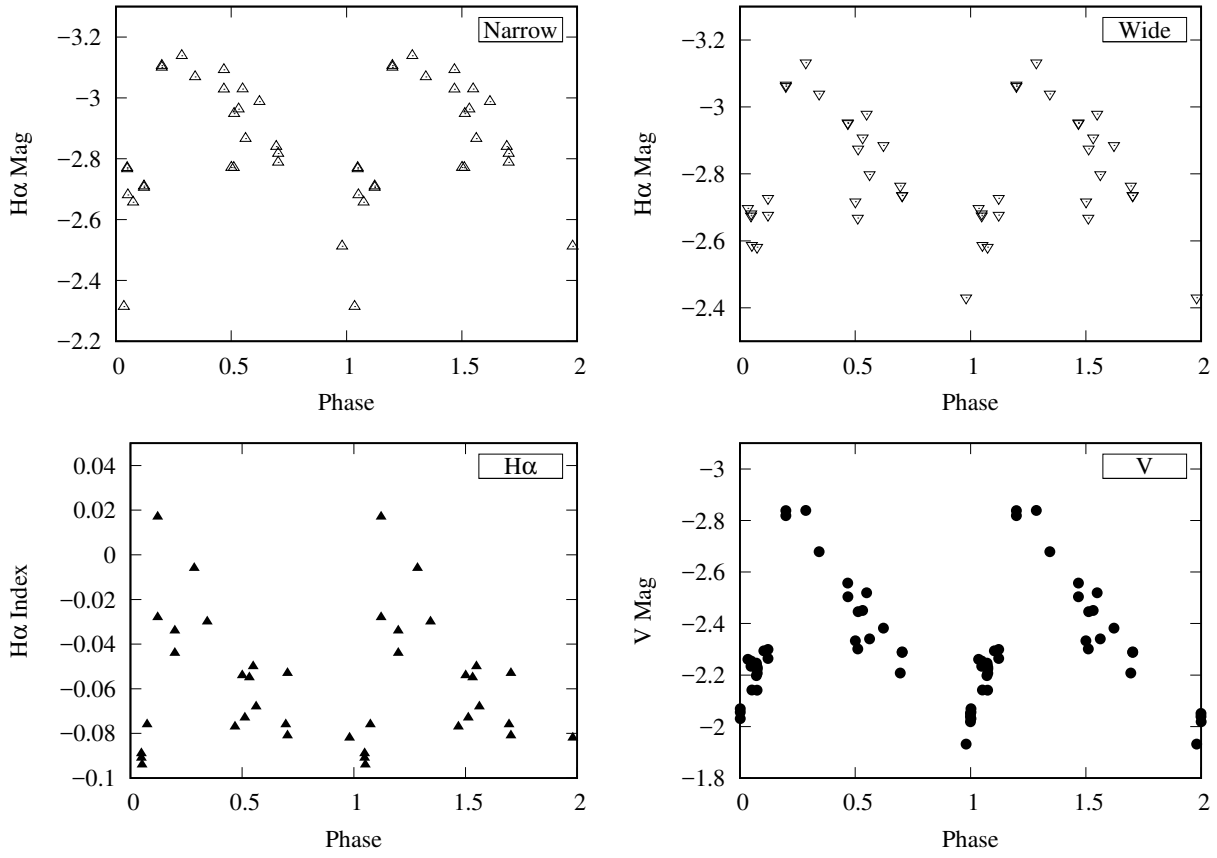

Figure 3.12 Differential light curves of TT Aql

3.1.11 TT Aql

TT Aql's differential curve in V, while sloppier than most other Cepheids studied, still clearly shows oscillation (cf. Fig. 3.12). Its Hα filter curves, however, are questionable. Measurements of phase 0.2–0.7 seem to indicate a steady decrease in brightness in both filters, but the reliability of observations at other points in the curve is unclear. Nonetheless, the Hα index curve shows a weak oscillatory nature. TT Aql was one of the brightest Cepheids observed, with an average V magnitude of 7.19 and relatively high oscillation amplitude (cf. Table 2.1). The lack of a clearer pattern in Hα from such a bright star is disappointing.

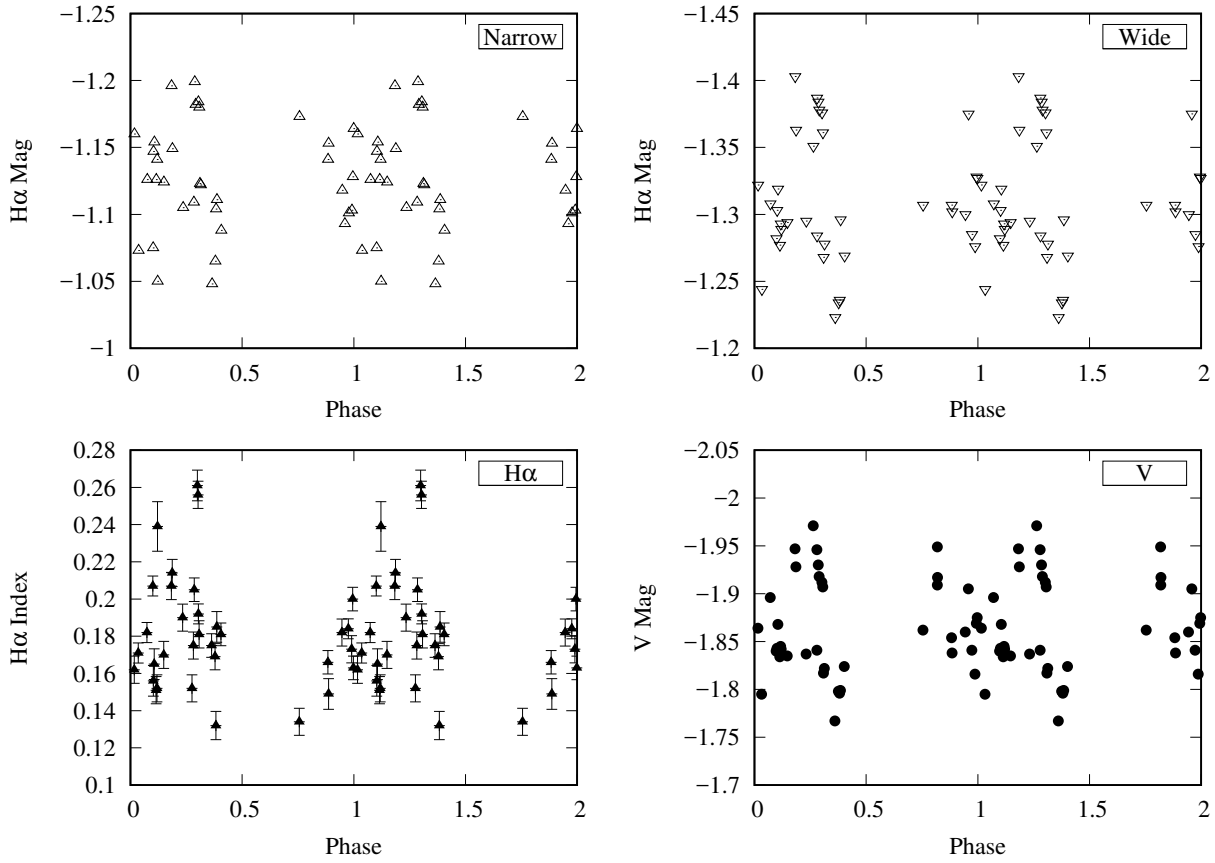

Figure 3.13 Differential light curves of TYC 1033-3220-1

3.1.12 TYC 1033-3220-1

Unlike any of the Cepheids heretofore discussed, TYC 1033-3220-1 showed no discernible pattern in any filter (cf. Fig. 3.13) when phased with the period from Berdnikov et al. (2009). This may be because the amplitude of oscillation is too low for our telescope to observe; Berdnikov et al. (2009) list the star as a low-amplitude Cepheid. Another possibility is that the period is incorrect. To investigate this, I attempted to find a new period through Least-Squares Spectral Analysis, detailed below in section 3.2.

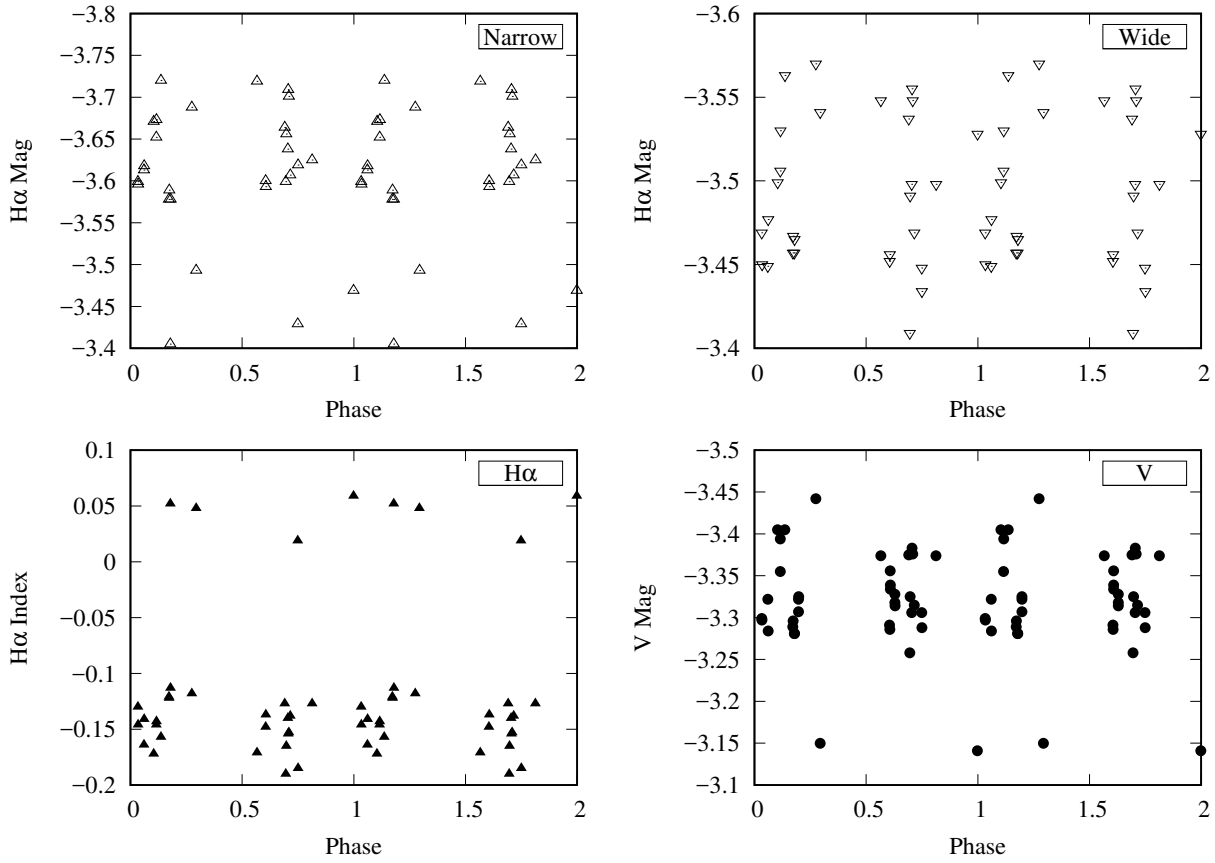

Figure 3.14 Differential light curves of V1452 Aql

3.1.13 V1452 Aql

V1452 Aql presented the same problem as TYC 1033-3220-1; phasing it with the period from the GCVS yielded no evident pattern (cf. Fig. 3.14). The GCVS give no indication of the star's amplitude, so it may oscillate on too small a scale to observe. The Hipparcos mission (ESA 1997) recognized it as a variable star but left it unresolved, without a period. Because I was unable to reproduce a clear light curve using the period from the GCVS, I again tried to find a period through LSSA (cf. section 3.2).

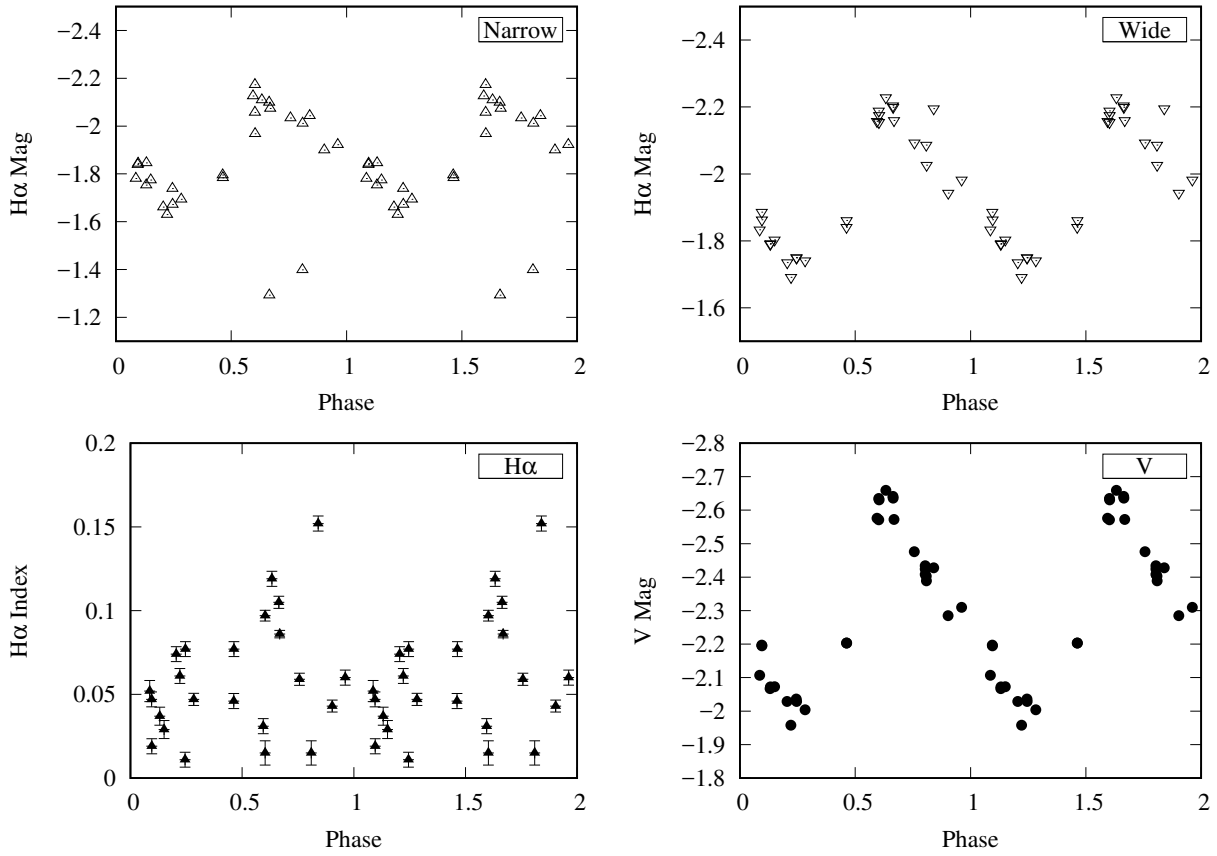

Figure 3.15 Differential light curves of VZ Cyg

3.1.14 VZ Cyg

VZ Cyg fell victim to the same fate as most of the Cepheids presented—while the V filter and wide Hα filter show decent light curves, the narrow Hα filter's lower S/N confuses the derived Hα index values (cf. Fig. 3.15). Thus the index curve, while it shows some evidence of oscillation, does not consistently track the strength of the spectral line.

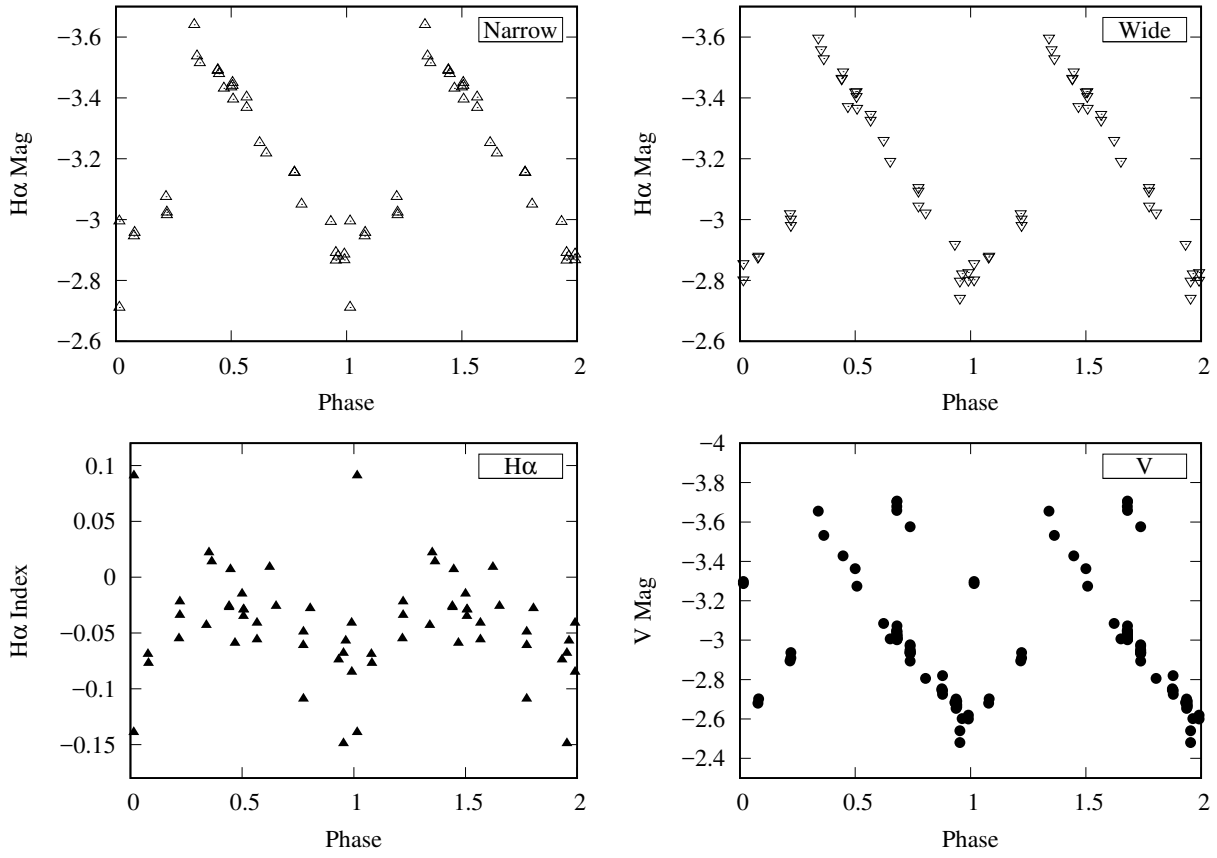

Figure 3.16 Differential light curves of X Cyg

3.1.15 X Cyg

As the genesis of this study, it is not surprising that X Cyg produced one of the clearest Hα index curves (cf. Fig. 3.16). X Cyg was also the first target studied to test the telescope system. Those initial test observations were taken in V and were lower quality than those taken later. This may be an explanation for the unexpected scattered points in the differential V curve. Once observations began in earnest, however, it produced extremely clear curves in both the wide and narrow Hα filters. Evidence of regular oscillation in the Hα index can clearly be seen as well.

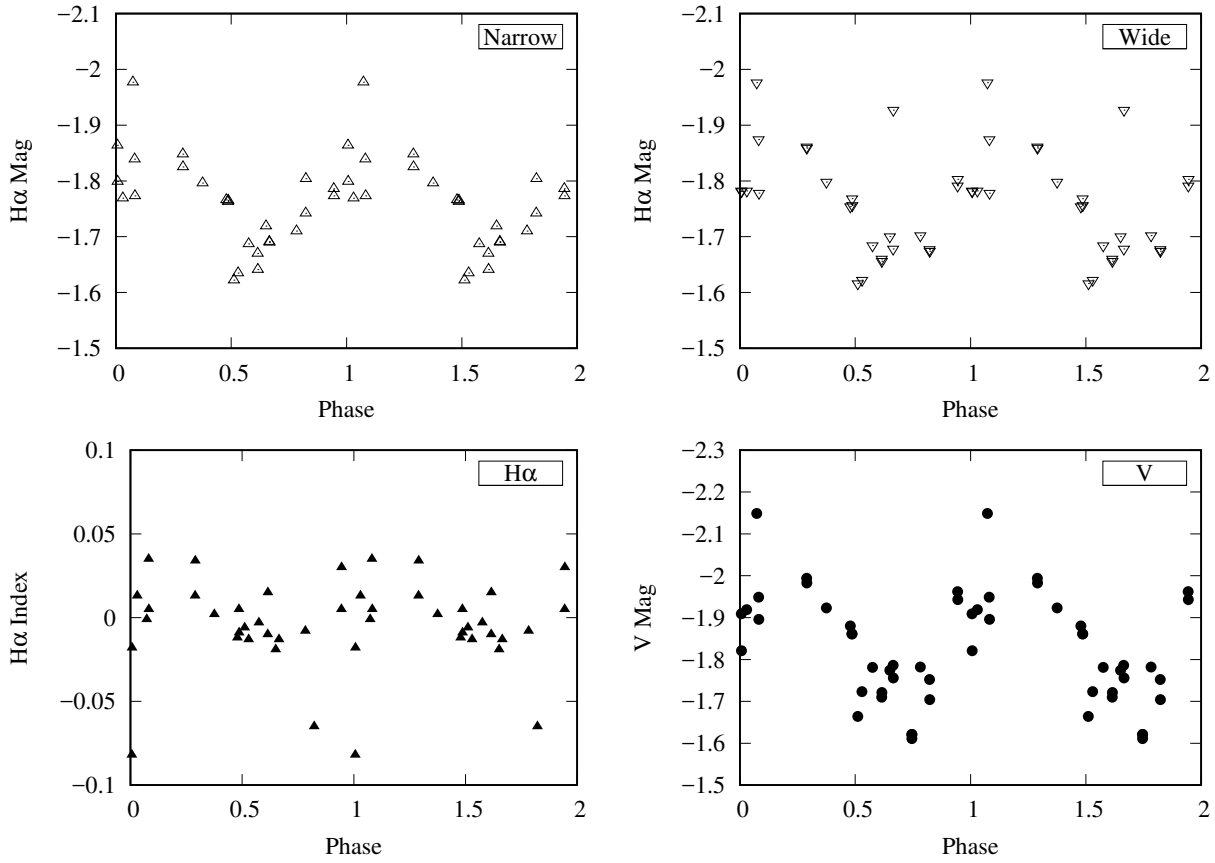

Figure 3.17 Differential light curves of X Lac

3.1.16 X Lac

At first glance, the scatter in the light curves of X Lac (cf. Fig. 3.17) suggests that its Hα index curve would be meaningless. However, the index curve seems to show some regular pulsation despite the noise in the curves. Perhaps most interesting is the unexpected cleanness of the narrow filter curve vis-à-vis the wide filter. The most likely explanation is that the exposure length for the wide filter was set to short. Ironically, observations in the opaquer of the two filters had higher S/N.

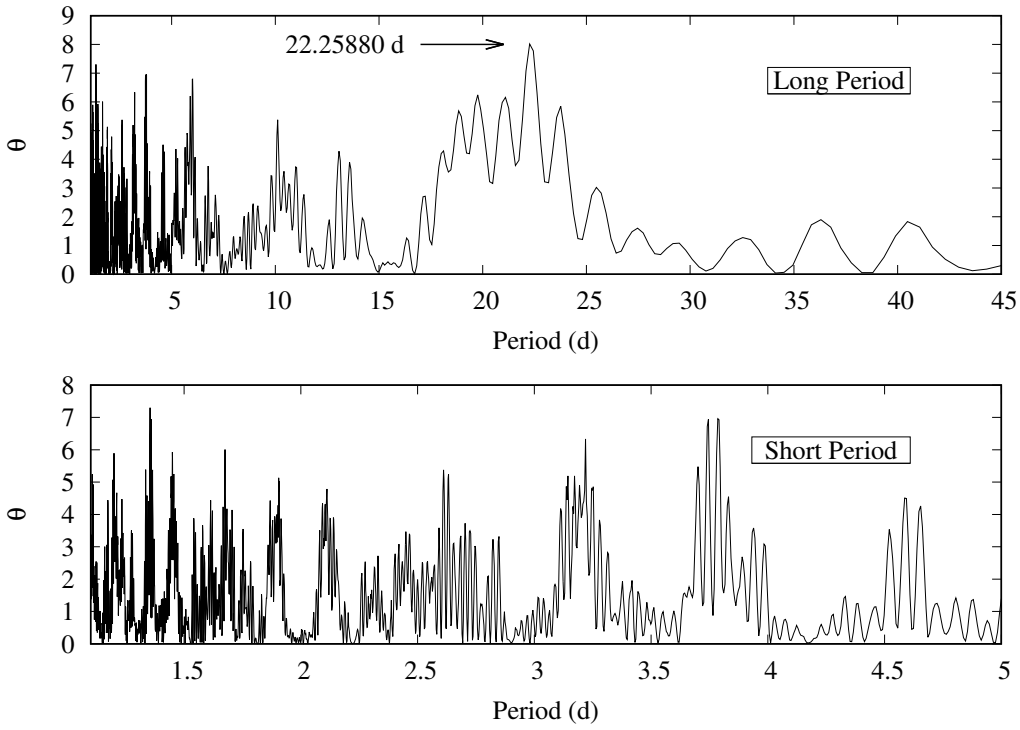

Figure 3.18 Lomb-Scargle periodogram of TYC 1033-3220-1 over a range of periods from 1.1 days to 45 days. The second periodogram is restricted to a range up to 5 days to better show the results for short periods. The most likely periods found for TYC 1033-3220-1 were 22.25880 days, 1.35417 days, and 3.78558 days.

3.2 Period determination

In this section I present the results of LSSA[1] in the form of Lomb-Scargle periodograms for several of the Cepheids in this study. I then present and discuss the newly phased data using the strongest periods from these periodograms.

3.2.1 TYC 1033-3220-1

As mentioned in Section 3.1.12, I attempted to determine the period for TYC 1033-3220-1 when it phased poorly. Figure 3.18 shows the Lomb-Scargle results from Peranso for TYC 1033-3220-1

[1] cf. Sec. 2.7

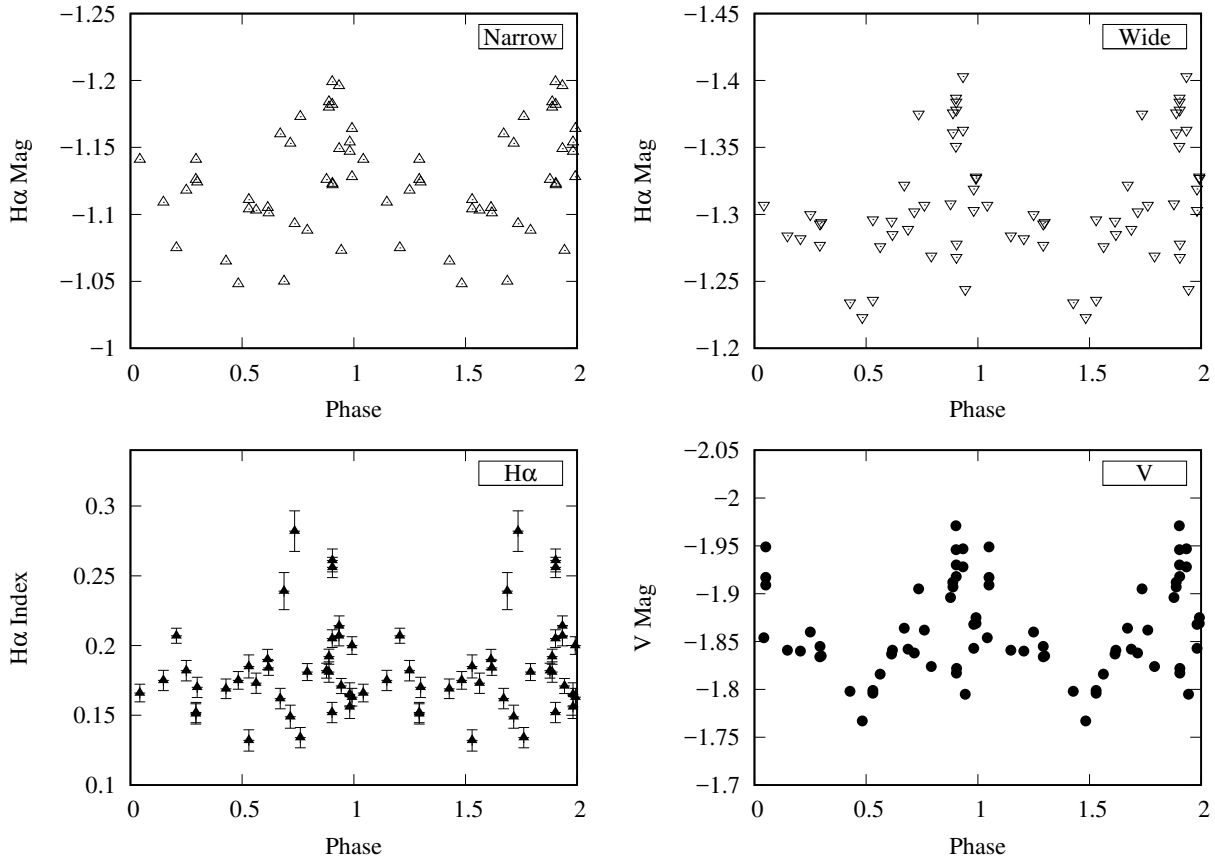

Figure 3.19 Differential light curves of TYC 1033-3220-1 using a period of 22.25880 days

using the observations taken in the V filter. The most likely periods from the analysis are 22.25880 days, 1.35417 days, and 3.78558 days. None of the periods determined are particularly close to the 1.142982 day period reported by Berdnikov et al. (2009). In fact the large distribution of periods may be indicative of multiperiodicity in the star. However, the 22.25880 day period was the strongest result from the analysis. Using this period, I again phased the data to produce new light curves, shown in Figure 3.19. The improved light curves show clear evidence of pulsation in V. The Hα filters are by comparison more scattered, though at least in the wide filter, regular pulsation is apparent. Though the Hα index curve appears to show some variation, that may simply be the scatter in the measurements.

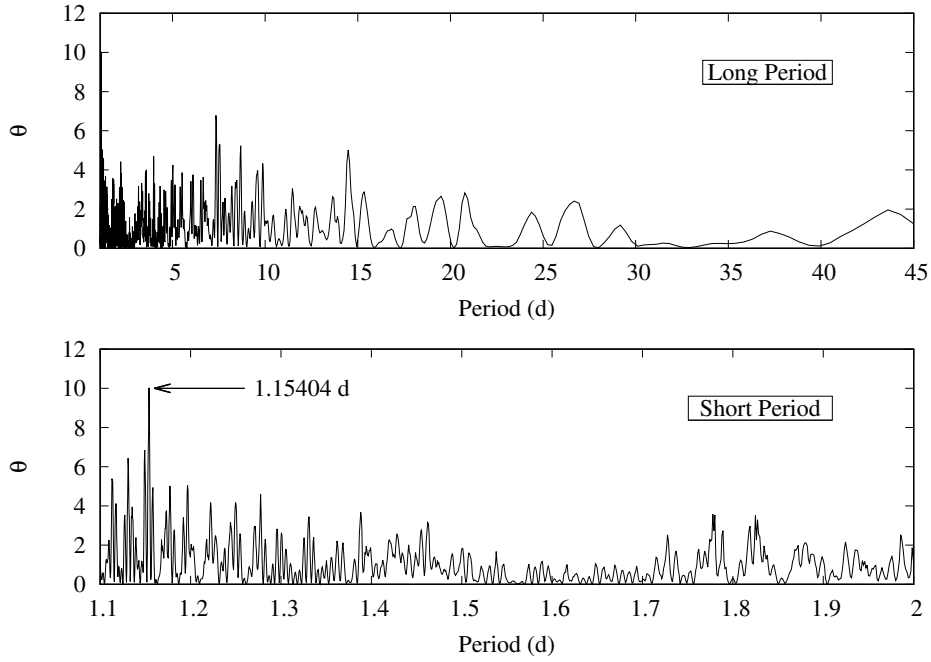

Figure 3.20 Lomb-Scargle periodogram of V1452 Aql over a range of periods from 1.1 days to 45 days. The second periodogram is restricted to a range up to 2 days to better show the results for short periods. The most likely periods found for V1452 Aql were 1.15404 days, 1.14933 days, and 1.13089 days.

3.2.2 V1452 Aql

After performing creating a Lomb-Scargle periodogram (cf. Fig. 3.20) from the observations in V, I determined a most likely period of 1.15404 days for V1452 Aql. Unfortunately, this did little to change the appearance of the light curves, as shown in Figure 3.21. Some extremely weak evidence of oscillation in the narrow Hα and V curves can be seen, but on the whole, the data appear as little more than a scatter plot. It is possible that V1452 Aql's amplitude is simply too small to detect.

3.2.3 EW Sct

EW Sct is a Cep(B) type, meaning it is a Cepheid that pulsates simultaneously in both the fundamental (P_0) and first overtone (P_1). Although its period was not listed in SIMBAD, a search

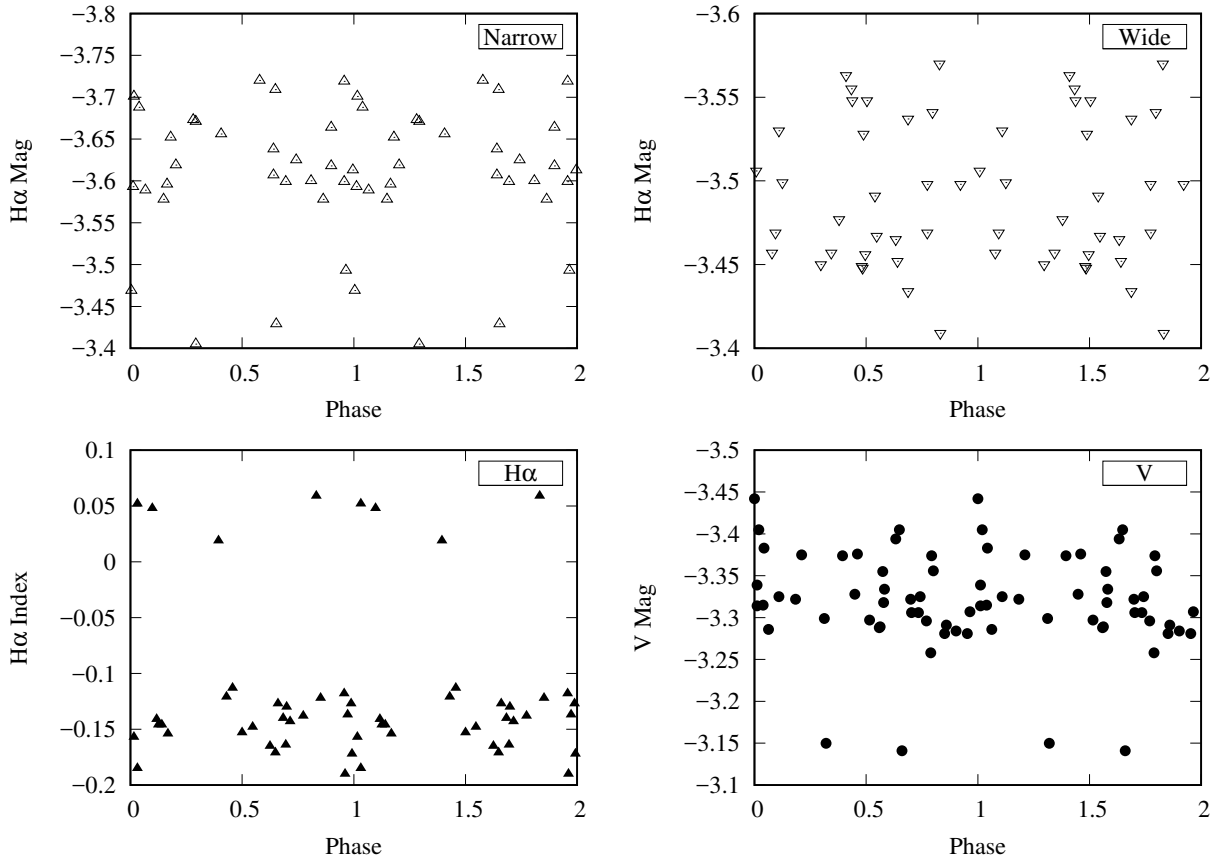

Figure 3.21 Differential light curves of V1452 Aql using period of 1.15404 days

through the literature revealed several other studies on the star. The Galactic Cepheid Database[2] (Fernie et al. 1995) lists a fundamental period for EW Sct of 5.8233 days. Kovtyukh et al. (2016) reported a fundamental period of 5.8235 days for EW Sct and a P_1/P_0 ratio of 0.6986. Sziládi et al. (2007) found the same results—a fundamental period of 5.8235 days for EW Sct and a P_1/P_0 ratio of 0.6986.

To attempt my own determination of EW Sct's period, I combined V filter observations from the 8-inch telescope at BYU with data retrieved from the AAVSO database. In total, 33 nights were taken from the AAVSO and used with the 15 nights from BYU, totaling 63 data points. Because I combined two separate data sets, I used Period04 to construct the periodogram (shown in Fig.

[2] http://www.astro.utoronto.ca/DDO/research/cepheids/table_physical.html

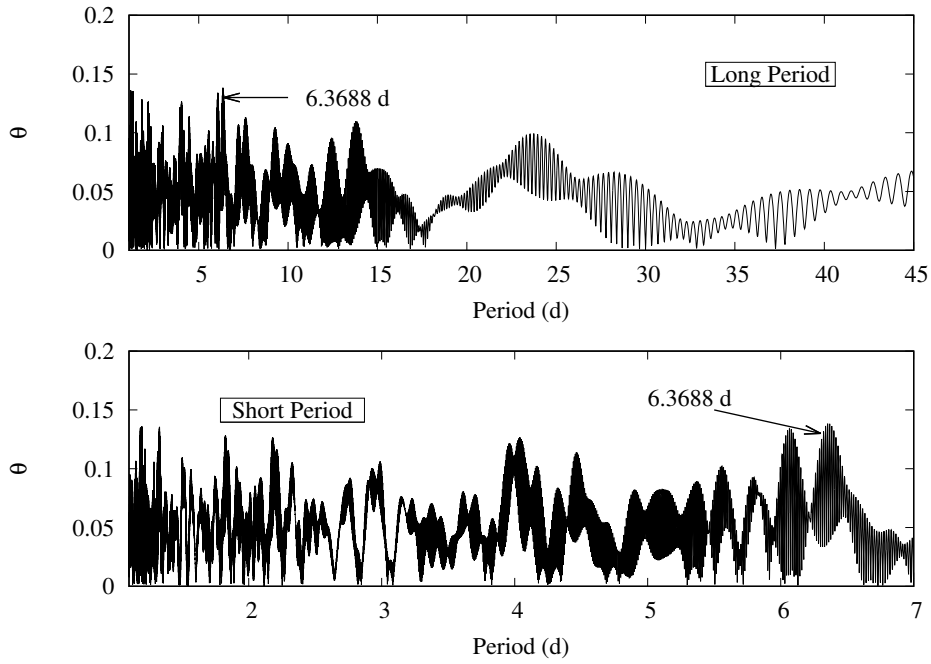

Figure 3.22 Periodogram of EW Sct over a range of periods from 1.1 days to 45 days. The second periodogram is restricted to a range up to 7 days to better show the results for short periods. The most likely periods found for EW Sct were roughly 6.36 days, 1.19 days, and 1.32 days. These are in poor agreement with the 5.823 day period by Fernie et al. (1995) and others.

3.22) instead of Peranso, as explained in Section 2.7. The most likely periods from the periodogram were roughly 6.36 days, 1.19 days, and 1.32 days. None of these periods match well with those reported previously—all ~ 5.823 days. Using the most likely period of $6.3688(\pm 0.00188)$ days for the fundamental, I determined a period for the first overtone of $4.043057(\pm 0.000738)$ days. This yielded a P_1/P_0 ratio of $0.634820(\pm 0.000478)$.

The discrepancy between the period I determined through LSSA and that reported in the literature is alarming. The most likely cause of such a large difference is the paucity of data. EW Sct was not observed in 2018, and having so few data points hindered the strength of the analysis. In addition, EW Sct's nature as a multimodal Cepheid inherently introduces scatter into its light curve. There is no one period that phases the data into a single, crisp curve. However, as shown in

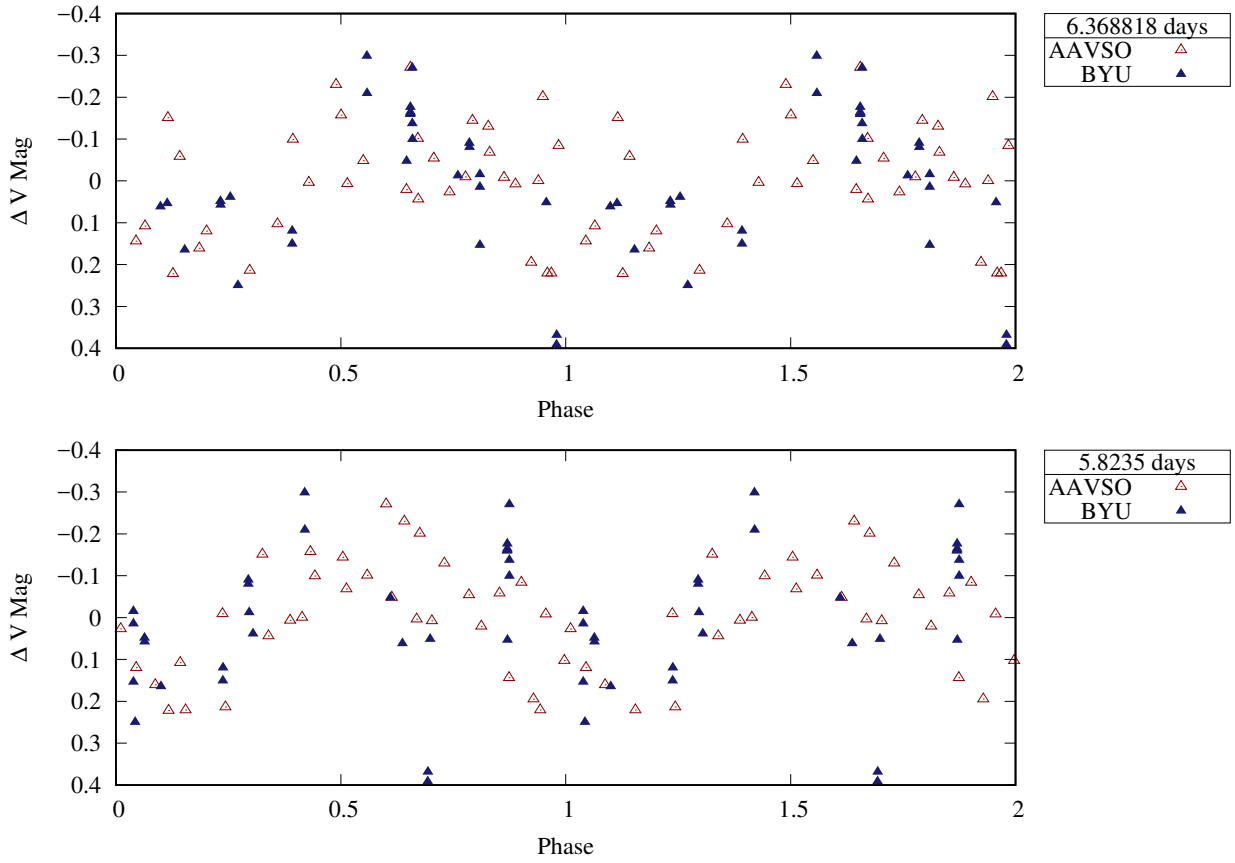

Figure 3.23 Comparison of light curves of EW Sct using two periods. The first uses a period of 6.368818 days, determined through LSSA of BYU and AAVSO data in the V filter. The second uses a period of 5.8235 days, taken from sources in the literature.

Figure 3.23, the quality of the light curve using the period I determined is not far from that using the period from the literature.

3.2.4 V2081 Cyg

V2081 Cyg was identified as a Cepheid by the Hipparcos mission in 1997 (ESA 1997). It was labeled as having a magnitude range between minimum and maximum light of about 0.06 mags in the Hp filter, a broadband filter specific to Hipparcos. However, it had no period listed in SIMBAD or in the GCVS. Upon further research, I found that the original Hipparcos catalogue listed a period

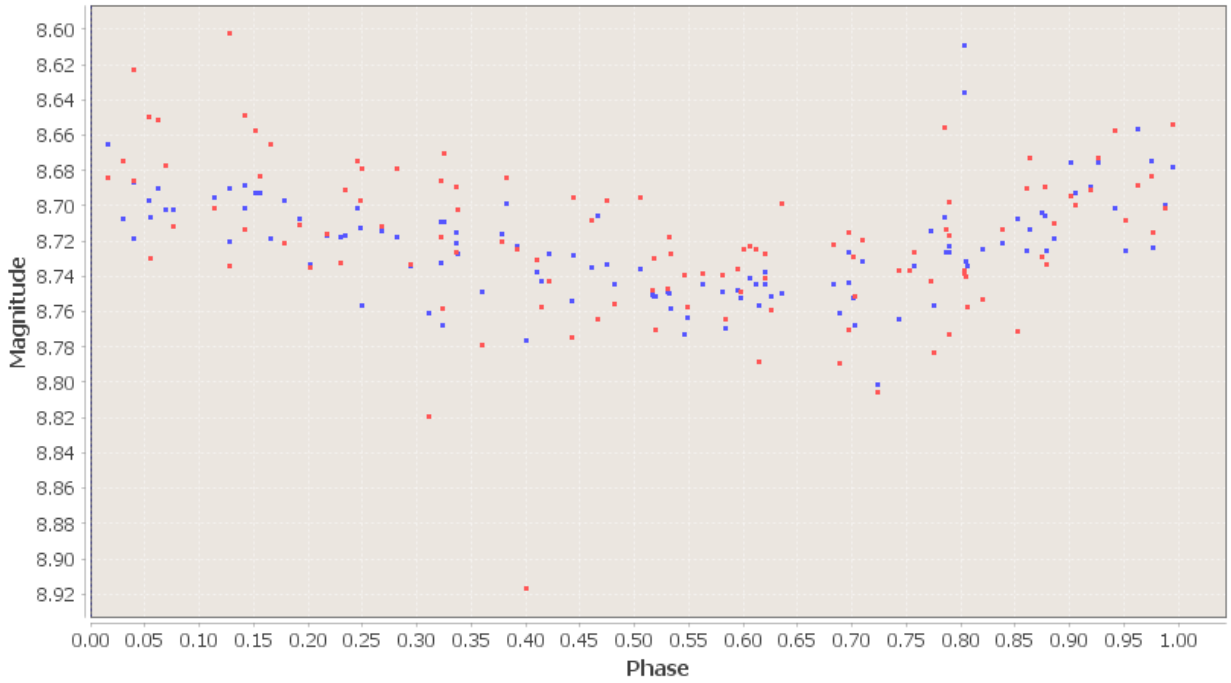

Figure 3.24 Light curve of V2081 Cyg from Hipparcos data (ESA 1997). Different colors represent different ways magnitudes were measured by instruments on Hipparcos and can be ignored.

for V2081 Cyg of 1.0023210 days. Periods close to the value of a single day are dubious, as typically observations are made each night, and the cadence of observations can produce an artificial artefact during LSSA. Furthermore, such a short period is atypical of Cepheids, indicating that V2081 Cyg may have been misidentified by Hipparcos.

However, the photometric data from Hipparcos' 108 observations of V2081 Cyg shown in Figure 3.24 clearly indicate regular variability for that period. The two colors in the figure represent different methods Hipparcos used to measure magnitudes; the difference between the two is not very important and can be ignored[3]. Because the period reported by Hipparcos is so close to a single day, I expanded the lower limit of periods when performing LSSA on V2081 Cyg from 1.1

[3]The Hipparcos satellite used a photon-counting image dissector tube device, whose mean level and amplitude (dc and ac components) could be used to produce magnitudes. Details can be found in Vol. 1 of the Hipparcos and Tycho Catalogues (ESA 1997).

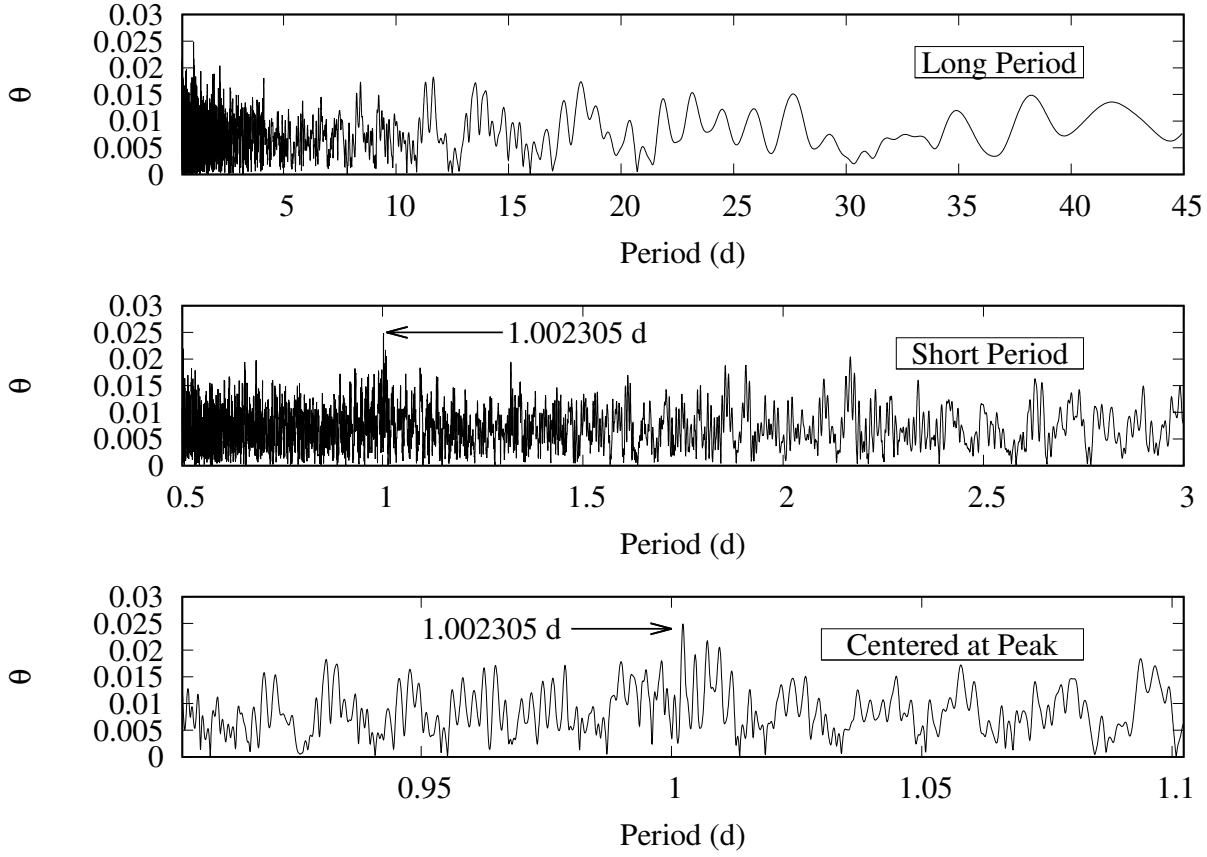

Figure 3.25 Lomb-Scargle periodogram of V2081 Cyg over a range of periods from 0.5 to 45 days. The second periodogram is restricted to a range up to 2 days to better show the results for short periods. The final periodogram is centered even further at the peak period of $1.002305(\pm 0.000053)$ days. This is in agreement with the period reported by Hipparcos (ESA 1997).

days to 0.5 days. As with EW Sct, I also combined BYU observations with data taken from the AAVSO. In total, 24 nights from BYU were combined with 127 nights from the AAVSO, yielding 489 observations. The resultant periodogram is shown in Figure 3.25. The most likely period from the analysis was $1.002305(\pm 0.000053)$ days; the period reported by Hipparcos is within error bars of this result. Phasing the data with this period, I created a light curve of the V observations, shown in Figure 3.26. Like the Hipparcos data, the BYU and AAVSO observations also indicate clear signs of variability using the same period.

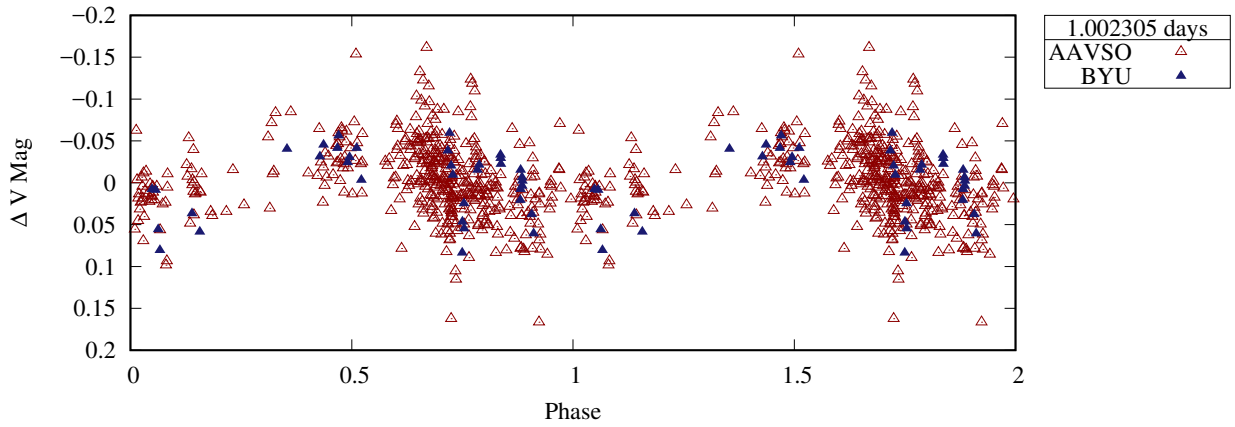

Figure 3.26 Phased light curve of V2081 Cyg using a period of 1.002305 days, determined via LSSA.

The greatest advantage of V2081 Cyg over EW Sct in properly determining the period was the abundance of available data. By comparison, V2081 Cyg had far more observations (489) than did EW Sct (63). Having so many data points increased the effectiveness of LSSA and drove the error down. In addition, the residuals of V2081 Cyg when phased show no indication that it is multimodal, as EW Sct is. Thus, a single period is in theory all that is required to phase the data into a clear light curve. Still, it is encouraging to see the excellent agreement between Hipparcos data and BYU/AAVSO data.

V2081 Cyg's curiously short period nonetheless raised some questions. Cepheids typically have longer periods, lasting up to a few months. Further, the low amplitude of variation (~ 0.06 mags) is also atypical for a Cepheid (cf. Table 2.1). Further investigation revealed that V2081 Cyg's initial classification as a Cepheid was errant. The International Variable Star Index[4] from the AAVSO was updated in 2015 to list V2081 Cyg not as a Cepheid, but as a γ Doradus star, a nonradial pulsator with amplitude less than 0.1 mag and period between 0.3 and 3 days.

[4] https://www.aavso.org/vsx/

3.3 Conclusions

The two goals of this project were (1) to take photometric measurements of the temperature of a collection of Cepheids, and (2) to demonstrate the capacity of small telescopes in urban environments to reproduce results from larger telescopes in isolated observatories. As seen in Section 3.1, the 8-inch telescope was certainly capable of reproducing decent light curves in the V filter for most of the Cepheids. The wide Hα filter also usually produced clear curves. However, the lower S/N of the narrow Hα filter introduced problems; to obtain enough signal, exposures had to run decidedly long. Because the telescope's tracking is not perfect, this introduced smearing of the images as the stars moved across the frame, impairing the quality of the data. The resultant Hα index curves, then, were incontrovertibly poor.

The final verdict, though unfortunate, may be that the 8-inch telescope simply lacks the light-gathering power necessary to make full use of the Hα filter system. If observations are taken in the V filter, the 8-inch can go no brighter than stars of magnitude ~ 6.5. However, even for stars this bright, the narrow filter requires surprisingly long exposure lengths. TT Aql, for instance, reaches magnitude 6.520 at brightest (cf. Table 2.1). To prevent overexposure, V filter exposure lengths were reduced to three seconds—the shortest exposure that does not introduce unwanted shutter effects from the camera. By comparison, the wide Hα filter exposure length was 12 seconds; the narrow, 75 seconds—25 times as long as the V exposures! Other fainter stars had narrow filter exposure lengths as long as between five and ten minutes, and still had poor S/N. Any exposures longer than ten minutes would distort the PSF of the stars too far, rendering the data ineffective. So, while the 8-inch telescope is effective with wide band-pass filters such as V, its use in narrow filters is significantly limited.

For the Cepheids whose pulsation period I attempted to determine, Least-Squares Spectral Analysis yielded mixed results. TYC 1033-3220-1 and V1452 Aql had periods listed in SIMBAD, but phasing with those periods produced poor light curves, even in V. However, rephasing with

new periods found through LSSA failed to significantly improve the curves (cf. Figs. 3.19 and 3.21). EW Sct had no period listed in SIMBAD, but the combination of scarcity of data during LSSA and the star's inherent multimodal nature made finding a period difficult. The period I found differed from that reported by others by about half a day, but the quality of the light curves using either period was comparable (cf. Fig. 3.23). V2081 Cyg, on the other hand, had an abundance of data available from the AAVSO. Combining that large data set with the 8-inch telescope's V filter observations yielded a tightly constrained period in good agreement with that found by Hipparcos. Regrettably, it turns out that V2081 Cyg is actually a γ Doradus star, misidentified as a Cepheid.

3.4 Directions for further work

In sum, the project partially completed its goals, but fell short in two ways. First, not enough data were taken. Inclement weather, technical difficulties, and a particularly bad haze of wildfire smoke covering Utah Valley for most of the summer of 2018 inhibited the number of nights available for observation. As the spectral analysis of V2081 Cyg shows, more data generally leads to lower errors and tighter results. Obtaining more high quality observations in all filters would likely reduce scatter in the phased light curves and augment the veracity of period determination through LSSA.

Second, the quality of narrow Hα exposures was too poor. I created the target list for the study by looking for Cepheids that are situated in an observable part of the sky and that would be as bright as possible without overexposing V filter observations of our minimum exposure length of three seconds. Sadly, in most cases, if the target was observable in V, it was too dim for the narrow Hα filter. In the end, many of the narrow Hα observations had lamentably low S/N, influencing the robustness of the Hα index measurements.

To remedy these errors, I recommend the study be continued and more data be collected, permitting the following caveats. To increase the S/N of narrow filter observations, one of two

options must be employed: (1) that the campaign be moved to a larger telescope, capable of collecting more light, or (2) that the emphasis be shifted to brighter targets, even if they are too bright to be observed in V. The 8-inch telescope's capabilities in wide band-pass filters has been well established, and V filter observations are no longer necessary to achieve the project goals.

I also recommend that in place of single-aperture photometry in IRAF or differential photometry in VPhot, multi-aperture nondifferential photometry be performed in IRAF or otherwise. Because the comparison ensembles remain unchanged between observations, the subtraction of differential measurements when determining Hα index ought to pose no problem. However, the filter system was designed with nondifferential magnitudes in mind, so that method may produce better results.

List of Figures

Bibliography

1997, The HIPPARCOS and TYCHO catalogues. Astrometric and photometric star catalogues derived from the ESA HIPPARCOS Space Astrometry Mission, Vol. 1200

Baker, N., & Kippenhahn, R. 1962, Zeitschrift für Astrophysik, 54, 114

Berdnikov, L. N., Kniazev, A. Y., Kravtsov, V. V., Pastukhova, E. N., & Turner, D. G. 2009, Astronomy Letters, 35, 311

Collins, K. A., Kielkopf, J. F., Stassun, K. G., & Hessman, F. V. 2017, AJ, 153, 77

Cox, J. P. 1985, in IAU Colloq. 82: Cepheids: Theory and Observation, ed. B. F. Madore, 126–146

Eddington, A. S., S. 1941, MNRAS, 101, 182

Engle, S. G., & Guinan, E. F. 2012, Journal of Astronomy and Space Sciences, 29, 181

Feast, M. W. 1996, Cepheid variables, ed. C. Jaschek & C. Sterken, Light curves of variable stars

Fernie, J. D., Evans, N. R., Beattie, B., & Seager, S. 1995, Information Bulletin on Variable Stars, 4148, 1

Gaia Collaboration. 2018, VizieR Online Data Catalog, I/345

Hearnshaw, J. B. 1986a, The interpretation of stellar spectra, The analysis of starlight: one hundred and fifty years of astronomical spectroscopy (40 West 20th Street, New York NY 10011, USA: Cambridge University Press), 208–254

—. 1986b, Spectral classification at Harvard, The analysis of starlight: one hundred and fifty years of astronomical spectroscopy (40 West 20th Street, New York NY 10011, USA: Cambridge University Press), 104–142

Hintz, E. 2019, Astrometry – The Simple Solution

Janesick, J., & Blouke, M. 1987, Sky & Telescope, 74, 238

Joner, M. D., & Hintz, E. G. 2015, The Astronomical Journal, 150, 204

Klagyivik, P., & Szabados, L. 2009, A&A, 504, 959

Kovtyukh, V., et al. 2016, MNRAS, 460, 2077

Leavitt, H. S., & Pickering, E. C. 1912, Harvard College Observatory Circular, 173, 1

Pickering, E. C. 1890, Annals of Harvard College Observatory, 27, 1

Saio, H., & Gautschy, A. 1998, ApJ, 498, 360

Samus, N. N., Kazarovets, E. V., Durlevich, O. V., Kireeva, N. N., & Pastukhova, E. N. 2017, Astronomy Reports, 61, 80

Schmidt, E. G., Hemen, B., Rogalla, D., & Thacker-Lynn, L. 2009, AJ, 137, 4598

Sterken, C., & Jaschek, C. 1996, The classification of variable stars, ed. C. Jaschek & C. Sterken, Light curves of variable stars

Sziládi, K., Vinkó, J., Poretti, E., Szabados, L., & Kun, M. 2007, A&A, 473, 579

Index